PASJ: Publ. Astron. Soc. Japan **59**, S77–S112, 2007 January 25

The Suzaku High Resolution X-Ray Spectrometer

Richard L. KELLEY,[1] Kazuhisa MITSUDA,[2] Christine A. ALLEN,[1] Petar ARSENOVIC,[1] Michael D. AUDLEY,[3] Thomas G. BIALAS,[1] Kevin R. BOYCE,[1] Robert F. BOYLE,[1] Susan R. BREON,[1] Gregory V. BROWN,[4] Jean COTTAM,[1] Michael J. DIPIRRO,[1] Ryuichi FUJIMOTO,[2] Tae FURUSHO,[2] Keith C. GENDREAU,[1] Gene G. GOCHAR,[1] Oscar GONZALEZ,[1] Masayuki HIRABAYASHI,[5] Stephen S. HOLT,[6] Hajime INOUE,[2] Manabu ISHIDA,[7] Yoshitaka ISHISAKI,[7] Carol S. JONES,[1] Ritva KESKI-KUHA,[1] Caroline A. KILBOURNE,[1] Dan MCCAMMON,[8] Umeyo MORITA,[7] S. Harvey MOSELEY,[1] Brent MOTT,[1] Katsuhiro NARASAKI,[5] Yoshiaki OGAWARA,[2] Takaya OHASHI,[7] Naomi OTA,[9] John S. PANEK,[1] F. Scott PORTER,[1] Aristides SERLEMITSOS,[1] Peter J. SHIRRON,[1] Gary A. SNEIDERMAN,[1] Andrew E. SZYMKOWIAK,[10] Yoh TAKEI,[2] June L. TVEEKREM,[1] Stephen M. VOLZ,[11] Mikio YAMAMOTO,[12] and Noriko Y. YAMASAKI[2]

[1]*NASA/Goddard Space Flight Center, Greenbelt, MD 20771, USA*
Richard.L.Kelley@gsfc.nasa.gov
[2]*Institute of Space and Astronautical Science (ISAS), Japan Aerospace Exploration Agency (JAXA), 3-1-1 Yoshinodai, Sagamihara, Kanagawa 229-8510*
[3]*Cavendish Laboratory, University of Cambridge, JJ Thomson Ave., Cambridge CB3 0HE, UK*
[4]*Lawrence Livermore National Laboratory, 7000 East Ave., L-260, Livermore, CA 94550, USA*
[5]*Quantum Equipment Division, Sumitomo Heavy Industries, Ltd., 5-2 Soubiraki-cho, Niihama, Ehime 792-0001*
[6]*Olin College of Engineering, Needham, MA 02492, USA*
[7]*Department of Physics, Tokyo Metropolitan University, 1-1 Minami-Osawa, Hachioji, Tokyo 192-0397*
[8]*Department of Physics, University of Wisconsin, Madison, WI 53706, USA*
[9]*RIKEN, 2-1 Hirosawa, Wako, Saitama 351-0198*
[10]*Department of Physics, Yale University, New Haven, CT 06511, USA*
[11]*NASA Headquarters, 300 E. Street SW, Washington, DC 20546-0001, USA*
[12]*Miyazaki Univeristy, 1-1 Gakuen Kibanadai-nishi, Miyazaki, Miyazaki 889-2192*

(Received 2006 September 1; accepted 2006 October 3)

Abstract

The X-Ray Spectrometer (XRS) has been designed to provide the Suzaku Observatory with non-dispersive, high-resolution X-ray spectroscopy. As designed, the instrument covers the energy range 0.3 to 12 keV, which encompasses the most diagnostically rich part of the X-ray band. The sensor consists of a 32-channel array of X-ray microcalorimeters, each with an energy resolution of about 6 eV. The very low temperature required for operation of the array (60 mK) is provided by a four-stage cooling system containing a single-stage adiabatic demagnetization refrigerator, a superfluid-helium cryostat, a solid-neon dewar, and a single-stage, Stirling-cycle cooler. The Suzaku/XRS is the first orbiting X-ray microcalorimeter spectrometer and was designed to last more than three years in orbit. The early verification phase of the mission demonstrated that the instrument worked properly and that the cryogen consumption rate was low enough to ensure a mission lifetime exceeding 3 years. However, the liquid-He cryogen was completely vaporized two weeks after opening the dewar guard vacuum vent. The problem has been traced to inadequate venting of the dewar He and Ne gases out of the spacecraft and into space. In this paper we present the design and ground testing of the XRS instrument, and then describe the in-flight performance. An energy resolution of 6 eV was achieved during pre-launch tests and a resolution of 7 eV was obtained in orbit. The slight degradation is due to the effects of cosmic rays.

Key words: instrumentation: detectors — X-rays: general

1. Introduction

Over the last decade there has been a revolution in the observational capabilities for studying celestial X-ray sources. Imaging, spectroscopy, and collecting area have improved dramatically through missions such as Einstein, ROSAT, ASCA, Chandra, and XMM-Newton. These X-ray observatories have led to a large number of discoveries with significant implications and relevance throughout astrophysics and cosmology. Along with the tremendous progress that has been made in developing high resolution X-ray optics with increasing collecting areas (e.g., Aschenbach 1988; Serlemitsos et al. 1995; Jansen et al. 2001; Weisskopf et al. 2002), a key component leading to the enormous progress has been the increase in capabilities for high resolution X-ray spectroscopy. Thus far, high spectral resolution, defined here as a few eV, has utilized dispersive spectroscopy, including Bragg spectrometers and transmission and reflection gratings. These devices offer very high spectral resolution for energies below about 1 keV (e.g., Canizares et al. 2000; Brinkman et al. 2000; den Herder et al. 2001), but the spectral resolving power decreases toward higher energies and also degrades

as the solid angle of the source being observed increases. Non-dispersive, photon-counting spectrometers have provided astrophysicists with powerful capabilities for moderate spectral resolution with high spatial resolution, with CCD's being the best example (e.g., Garmire 1999; Strüder et al. 2001; Turner et al. 2001; Koyama et al. 2007). However, these devices all use charge collection as the essential detection principle and have spectral resolution limited by the statistics of charge generation, and thus well below what can be achieved with dispersive spectrometers.

Starting in 1982, with the anticipated plans by NASA to develop the AXAF observatory (now Chandra), members of this team embarked on new ways to utilize semiconductors with energy band gaps smaller than Si or Ge to improve the energy resolution by increasing the number of electrons per event. This inquiry led to the consideration of narrow-gap materials that were used in infrared detectors and, ultimately, to the thermal detection of X-ray photons using bolometric principles and techniques well-known to infrared astronomy. The tremendous potential of the calorimetric approach was quickly realized by Moseley, Mather, and McCammon (1984), who developed the concept and demonstrated that a resolution in the electron-volt range was possible with semiconductor thermometers and small pixels ($< \mathrm{mm}^2$) operated below $\sim 100\,\mathrm{mK}$. An X-ray microcalorimeter can be made to have high quantum efficiency over a large energy band along with nearly constant energy resolution. The spectral resolving power thus increases toward high energies, making it an ideal complement to the dispersive spectrometers. This makes the sensor particularly powerful for quantitative diagnostics, including velocity measurements, of elements heavier than Si, and especially the ubiquitous Fe K lines around 6 keV. Furthermore, an array of microcalorimeters can be used to create an imaging spectrometer for the study of extended sources without loss of spectral resolution. Following proof-of-principle work and a proposal to implement a microcalorimeter spectrometer for the AXAF observatory, the high resolution X-Ray Spectrometer (XRS) was eventually selected for flight development. For the next seven years or so, substantial progress was made on the detectors and cryogenic system required for maintaining the detector below 100 mK for several years in orbit.

In 1993, after a restructuring of the AXAF program and plans in Japan to develop a powerful new X-ray observatory, it was mutually decided by NASA and the Institute of Space and Astronautical Science (ISAS)[1] to incorporate the XRS into the Astro-E mission. The XRS would provide the high spectral resolution for the mission, complementing the grating spectrometers on Chandra and XMM-Newton (figures 1 and 2), while the other instruments on Astro-E would provide larger field of view and collecting area (the XIS: Koyama et al. 2007), and extend the bandpass to very high energies with much higher sensitivity (the HXD: Takahashi et al. 2007). The XIS would also continue to operate after the cryogens in the XRS were exhausted, enabling imaging with moderate spectral resolution for the full life of the mission. Within about a year

[1] ISAS was reorganized in 2003, and is now a part of Japan Aerospace Exploration Agency (JAXA).

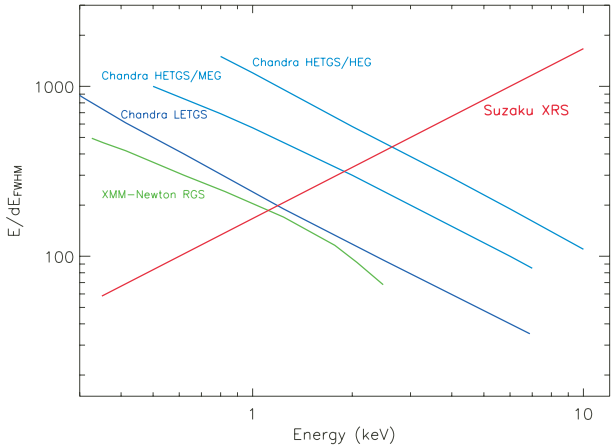

Fig. 1. Spectral resolving power of the XRS in comparison with the high resolution spectrometers on the Chandra and XMM-Newton observatories. These missions utilize dispersive gratings that provide very high resolution at low energies. The nearly constant energy resolution of the X-ray microcalorimeter with energy provides increasing spectral resolving power towards higher energies.

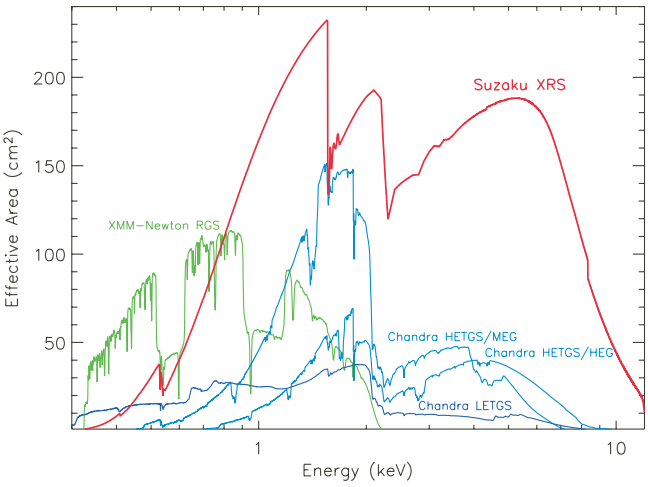

Fig. 2. Effective area of the XRS in comparison with the high resolution spectrometers on the Chandra and XMM-Newton observatories. The high intrinsic quantum efficiency of the microcalorimeter, coupled with the large throughput of the Suzaku X-Ray Telescope (Serlemitsos et al. 2007), provides large effective area for enabling high sensitivity spectroscopy.

the XRS was redesigned and a new version emerged based on a joint design with major components to be contributed by NASA and ISAS. By 1999 the instrument was completed and ready for flight. Astro-E was launched in 2000 February, but did not reach orbit due to a malfunction of the first stage rocket nozzle. Very soon after that event, proposals were successfully made to the respective national space agencies to rebuild the observatory with the same instruments for a new mission, Astro-E2. This mission has now been successfully launched, renamed Suzaku, and is currently in operation carrying out observations proposed from around the world (Mitsuda et al. 2007).

During the first few weeks after launch, the XRS performed essentially perfectly and was apparently on its way to

a multi-year science program. But before the instrument could be fully deployed, the He cryogen was vaporized after only about a month in orbit. The cause of this event has been investigated in Japan and in the US, and the reason for the loss is now understood to be the result of how the dewar was accommodated on the spacecraft. Although this preempted the use of the XRS for astrophysics, there was sufficient time to establish that the XRS, as a subsystem, worked extremely well and that the new technologies of X-ray microcalorimeters and sub-100 mK cooling may now be considered space-qualified.

The subject of this paper is the design, ground testing, and in-flight performance of the XRS instrument. Before describing the XRS, however, we very briefly mention other work that utilizes similar X-ray microcalorimeter array technology for both astrophysics and related laboratory work that has already produced significant scientific results. In parallel with the development of the XRS, work was begun in the early 1990's on a suborbital payload to measure the spectrum of the diffuse X-ray background below about 1 keV. This payload, the X-Ray Quantum Calorimeter (XQC), has been flown several times and has produced the first celestial X-ray spectrum with a microcalorimeter (McCammon et al. 2002). More recently, members of this team and other groups have used X-ray calorimeter technology for laboratory work, including atomic and nuclear physics, using electron-beam ion traps (Beiersdorfer 2003; Beiersdorfer et al. 2003; Brown et al. 2006a, b; Chen et al. 2005; Porter et al. 2004, 2005; Silver et al. 2002). Based on the success and the ultimate potential of this technology, and now the operation of the XRS microcalorimeter in space, much larger missions are being formulated that will have larger arrays, enabled further by alternate thermometer and read out schemes (Irwin 2002; Kilbourne et al. 2004), that should permit much larger fields of view. These include the Japanese New X-ray Telescope (NeXT: Takahashi et al. 2006), the NASA Constellation-X Mission (White et al. 2004), and the ESA/JAXA XEUS mission (e.g., Bavdaz et al. 2005).

2. Instrument Overview

The concept underlying the microcalorimeter is based on the very definition of energy — the energy of a light (or particle) quantum is inferred from the temperature increase of a thermometer in quasi-static equilibrium with an absorbing heat capacity. Actual devices consist of three basic elements: an X-ray absorber, a thermometer, and a link to a stable heat sink. A thermometer scheme that is commonly used is temperature-dependent resistance, such as of a doped semiconductor or a superconductor operated in its phase transition. At very low temperatures ($\lesssim 0.1$ K), the heat capacity, Johnson noise of the thermistor, and thermal fluctuations ("phonon noise") between the thermistor and heat sink can be made low enough that the amplitudes of heat pulses from individual X-rays can be sensed to better than a part in a thousand (Moseley et al. 1984; Stahle et al. 1999; McCammon 2005). Real devices have varying limitations, such as additional noise terms associated with the particular fabrication or choice of materials, position-dependent response, and the limited availability of materials that thermalize X-rays efficiently without contributing excessive heat capacity. However, it is possible to quantify these non-ideal effects and design a detector that is optimized for a particular energy resolution and quantum efficiency. The goal of the XRS was to produce a microcalorimeter array with an energy resolution of 12 eV or better at 6 keV in order to allow nearly complete resolution of the "triplet" line complex of He-like iron as a primary goal. The necessity for an array of microcalorimeters was set by the requirement to cover a useful field of view ($\sim 10\,\mathrm{arcmin}^2$) yet remain within a heat capacity budget low enough to permit this resolution. Over a period of about a decade, work centered on producing devices that have this resolution with a high degree of uniformity over an array of 32 individual microcalorimeter pixels with size $\sim 0.4\,\mathrm{mm}^2$. For the XRS, the most straightforward path toward this was to use micromachined silicon as the basis of the array, with ion-implanted Si as the thermometer (i.e., a thermistor), and use the semi-metallic crystal mercury telluride (HgTe) as the X-ray absorber (Kelley et al. 1993).

The implementation of a microcalorimeter spectrometer for Suzaku required a robust cooling system capable of cooling the sensor to 60 mK for a period of at least 2 years in order to carry out a comprehensive scientific observing program. This required a cryogenic system with extremely low heat loads that would fit within a volume of $\lesssim 1\,\mathrm{m}^3$. To meet these constraints, a four stage cooling system was developed jointly by NASA/Goddard, the University of Wisconsin, ISAS, and the Sumitomo Heavy Industries (SHI), Ltd. (Volz et al. 1996; Mitsuda, Kelley 1999; Kelley et al. 1999). Figure 3 shows a diagram of the major components of the XRS.

The detectors are located in the Front End Assembly (FEA). This unit provides the mechanical and thermal support for the array, an anticoincidence detector, and an initial stage of amplification based on JFET's. The detector box, referred to as the Calorimeter Thermal Sink (CTS), completely encloses the array and has a lid that supports one of the five blocking filters described below. Also mounted to the lid is a collimated calibration source that illuminates a special pixel located on the frame of the array, but outside of the field of view of the main array. The CTS has gold straps exterior to the enclosure that are used for thermal attachment to the next stage. This is a conventional, single-stage, adiabatic demagnetization refrigerator (ADR: e.g., Serlemitsos et al. 1990; Porter et al. 1999). The ADR is suspended within a $1\,\mathrm{T\,A}^{-1}$ superconducting magnet that is immersed in a 33-liter liquid He cryostat. The ADR is capable of cooling to below 50 mK, but in practice is controlled at 60 mK so that there is sufficient cooling power available to maintain this temperature for at least 24 hours. The ADR requires a heat sink to absorb the heat of magnetization, and for this the He bath is pumped by space to about 1.3 K (below the superfluid transition temperature of 2.2 K). To achieve the design requirement of a 2 year lifetime (and possibly the goal of 3 years), the net heat load into the He cryostat was required to be less than 1.0 mW assuming the cryostat were 90% full at the beginning of the mission.

To reduce the external heat loads on the helium, the cryostat is mounted within a ~ 120 liter toroidal dewar that contains solid neon, which is also space-pumped to a temperature of about 17 K. There is a single stage Stirling cycle cooler that provides cooling power to the outer-most of the vapor-cooled

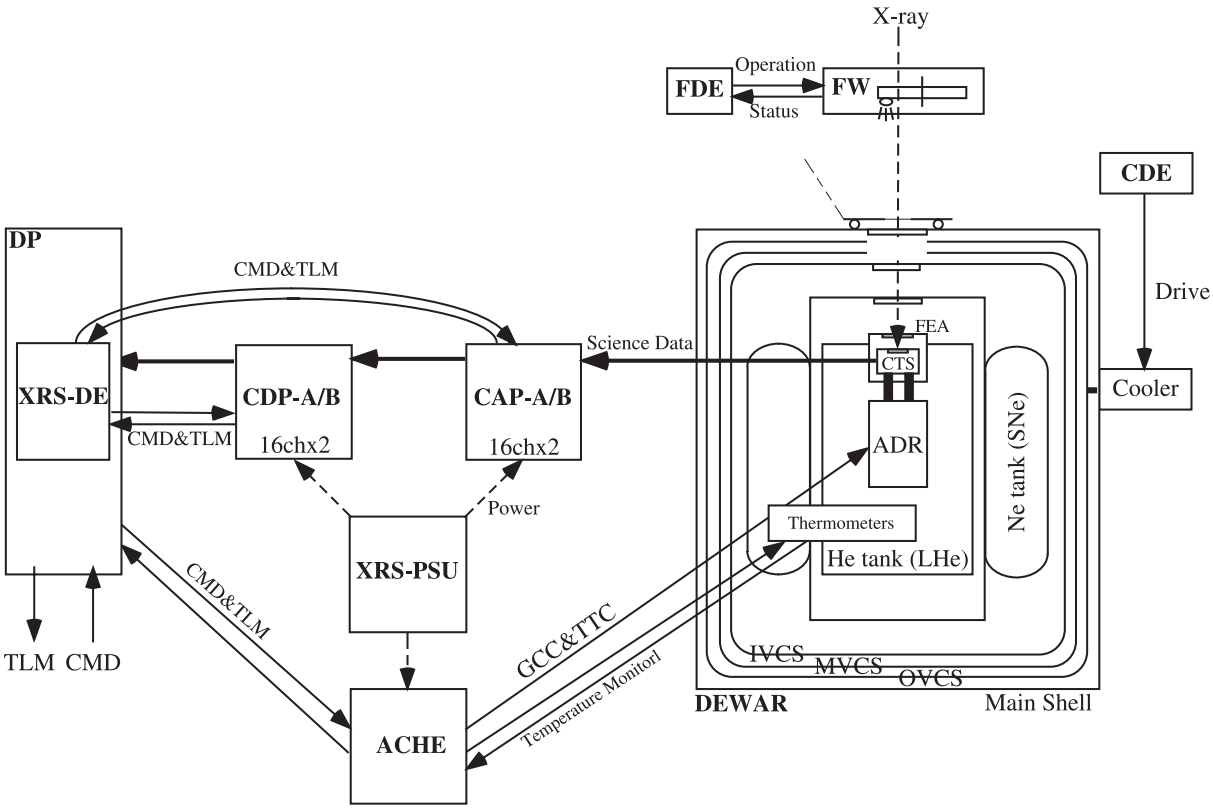

Fig. 3. XRS subsystem functional block diagram.

shields. This was added for Astro-E2 in order to increase the cryogen lifetimes. Careful attention to thermal isolation, controlling superfluid film flow, heat sinking, and staging of components to minimize parasitic heat loads were all required, along with keeping the system as modular as possible and able to survive the demanding launch loads of the M-V rocket.

The microcalorimeters are by their nature highly sensitive to essentially all forms of electromagnetic and particle radiation, so proper isolation from structures at higher temperature was necessary. This required the development of aluminized plastic filters that are thin enough to transmit X-rays (above about 0.3 keV) yet strong enough to survive a few torr differential pressure, repeated thermal cycling to cryogenic temperatures, and substantial random mechanical vibration and shock loads. The aperture is closed out with a series of four additional blocking filters that are attached to various thermal stages of the dewar. Just outside the aperture of the dewar, but attached to the spacecraft, is an external filter wheel (FW) that contains a series of filters designed to attenuate the flux from very bright sources, and also several radioactive X-ray sources for in-flight calibration.

The calorimeter and anticoincidence detector signals are amplified by the Calorimeter Analog Processor (CAP) and then processed for pulse height, arrival time, and other information by the Calorimeter Digital Processor (CDP). The CDP then sends telemetry to and receives commands from the XRS Digital Electronics (XRS-DE). The ADR Control and Housekeeping Electronics (ACHE) operates the ADR and reads out all thermometry within the dewar. Power to the XRS is provided by the XRS Power Supply Unit (XRS-PSU).

The He Insert, consisting of the He cryostat, ADR, detector assembly, blocking filters, and instrument electronics, was the responsibility of Goddard. The University of Wisconsin supplied the flight ADR salt pill. The Ne dewar, including Stirling-cycle mechanical cooler, was developed at SHI under the direction of ISAS. The other electronics boxes (power and telemetry/commanding) were provided through ISAS, and the filter wheel was developed at the Tokyo Metropolitan University and ISAS. The ground calibration of the instrument was done at Goddard, SHI, and ISAS.

In the remainder of this paper, we will successively go through the major components of the XRS, starting with the detector array and ending up with the electronics, and then discuss the performance of the XRS in the laboratory and in orbit.

3. XRS Detector System

3.1. The Microcalorimeter Array

The XRS microcalorimeter array uses ion-implanted Si for the thermometers. The Si is implanted to a carrier density just below the metal-insulator transition in order to achieve a very high temperature coefficient of resistance at low temperatures. Silicon etching is used to form the thermally isolating support beams to the heat sink. Finally, HgTe is manually attached to each pixel to absorb and thermalize X-rays. Discussion of the development of the Suzaku/XRS array design can be found in Stahle et al. (2003), and details of the new fabrication process

are in Brekosky et al. (2004). In this paper, we provide a brief description of the design and fabrication method.

The process starts with a silicon-on-insulator (SOI) wafer, which consists of a thin layer of silicon separated from the bulk silicon substrate of the wafer by a very thin oxide buffer. This buried oxide serves as both an etch stop and a diffusion barrier. Reactive-ion etching (RIE) is used to create thermally-isolated pixels. RIE is a dry etch process that permits the etching of silicon into any shape that can be defined by means of photolithography. Deep-RIE etches (DRIE) through a 400-μm wafer with nearly straight side walls. Etching from the front creates patterns in the top 1.5-μm layer of silicon, and etching from the back up through the thick substrate to the oxide layer defines the suspended silicon membrane of each sensor. A photolithographically patterned structural polymer is used to create a controlled interface between the implanted Si and the absorber.

For the absorber attachment points, we formed four 10 μm-thick spacers of Nano^{TM} SU-8 on each pixel. SU-8 is a polymer that is patterned like photo-resist, but bonds strongly to silicon like epoxy. The thermistor was formed by doping with phosphorus (P) compensated with boron (B). The thickness of the top silicon layer of an SOI wafer determined the thermistor depth. After capping with an oxide, we implanted a single dose each of P and of B into the 1.5 μm-thick SOI layer. The wafer was then annealed at high temperature for an extended period of time to diffuse the dopants to a uniform density throughout the 1.5 μm depth, remove damage, and allow the dopants to occupy substitutional lattice sites. We eliminated the effects of lateral diffusion by implanting over an area larger than the thermistor area and then defining the thermistor edges with the etch. We used degenerately doped leads to contact the thermistor. A lower density implant was used on the membrane in order to limit the heat capacity of the thermal sensor; a heavier dose was used on the solid frame. The room-temperature resistivity of the lighter dose was $\sim 200\,\Omega$/square, and the heavier was $12\,\Omega$/square. The resistivities drop by less than a factor of 2 on cooling to 4 K.

The combination of SOI and RIE enabled the fabrication of silicon links of the desired thermal conductance and minimum resonant frequency while maintaining a compact design. Though the thermal conductance achieved in the flight design was about a factor of two higher than expected from scaling measurements of straight beams fabricated on previous generations of devices, the conductance was uniform across pixels, across arrays, and across different fabrication runs. The resulting exponential decay time was 3–4 ms, depending on bias. The finite thermal conductance of the link between absorber and thermistor contributed to this time constant; modeling indicated a fall time of 2 ms would have resulted with perfect thermal coupling between the absorber and thermistor.

Due to a concern that applying epoxy or SU-8 directly to the thin silicon of the thermistor element could result in strain-induced changes in its electrical properties, we added tabs to the edges of each thermistor and placed cylindrical spacers on the tabs. Figure 4 shows an optical image of an individual pixel with an electron micrograph inset of an SU-8 spacer. A benefit of this attachment technique is that the line response was greatly improved compared with previous techniques that had the absorber, or an intermediate spacer, attached directly to the thermistor volume. Each pixel now has a nearly perfect Gaussian response to monochromatic X-rays. An example of the line shape is shown in figure 5.

There is a small penalty for this attachment scheme, however. The thermal conductance between the absorber and

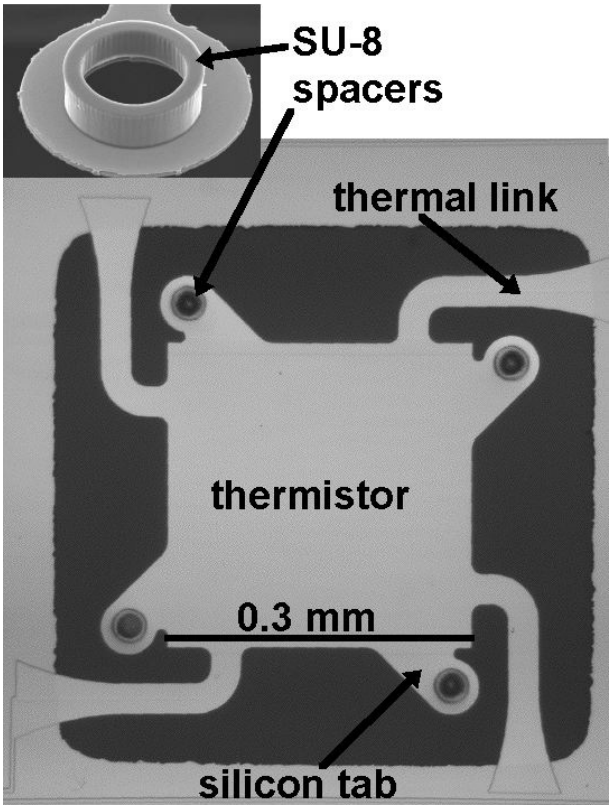

Fig. 4. Photos of a single XRS microcalorimeter thermometer. The square section is implanted to form the thermistor. There are four support beams and also four absorber "tabs" on which the HgTe absorber is subsequently attached. The thermistor area and support beams are 1.5 μm thick.

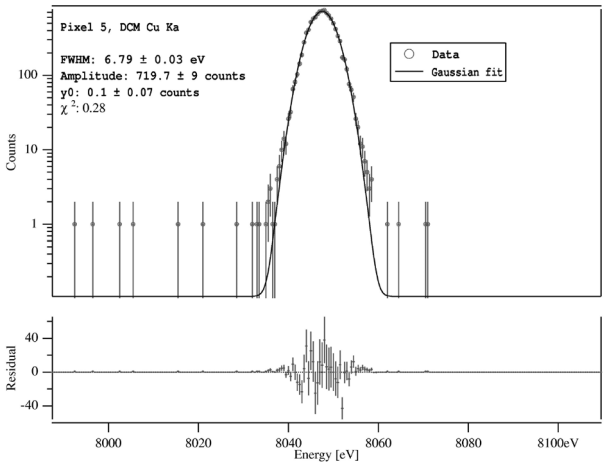

Fig. 5. XRS line spread function on a single pixel as obtained using X-rays from an X-ray monochromator tuned to Cu Kα.

the thermistor is nearly the same as that between the whole calorimeter and the heat sink. This degrades the signal-to-noise ratio because the detector response falls more steeply at high frequencies than the thermal fluctuation noise associated with the link to the heat sink. The internal thermal fluctuation noise that also results from this decoupling is not a factor because it is less than the Johnson noise at the sensitivity of the XRS detector. The range in pulse risetimes across the XRS array corresponds to $\pm \sim 30\%$ variation in the absorber-thermistor thermal conductance, and slightly higher resolution is clearly correlated with the faster risetimes. Modeling detector response across that range in risetimes predicts energy resolution ranging from 4.5 eV to 5.2 eV, compared with 4 eV if the absorber were perfectly coupled to the thermistor. The remaining difference between the predicted resolution and the measured resolution of typically 6 eV appears to be due to the thermal noise from X-rays hitting other pixels and the silicon around the array, which we will address later in the next section.

The HgTe was grown by DRS Infrared Technologies on CdZnTe wafers using molecular beam epitaxy. We removed the CdZnTe substrate completely using a wet etch, leaving free HgTe foils that we then diced mechanically to the appropriate size. We measured the heat capacity of our $624\,\mu\mathrm{m} \times 624\,\mu\mathrm{m} \times 8.5\,\mu\mathrm{m}$ HgTe absorbers as a function of temperature, and found $C(T) = 0.10\,(T/0.1\,\mathrm{K}) + 0.11\,(T/0.1\,\mathrm{K})^3$ pJ K^{-1}. The cubic term is consistent with a Debye temperature of 140 K. We attribute the linear term to an electronic heat capacity resulting from defects in the HgTe. The presence of Hg vacancies, for example, causes a p-type doping of the material and an associated electronic heat capacity term. This excess heat capacity is equal to the Debye term at ~ 0.1 K and is twice the Debye term at our biased operating point of ~ 0.074 K.

To attach the absorbers to the SU-8 tubes, we applied Emerson and Cuming Stycast$^{\mathrm{TM}}$1266 epoxy to the upper interior of each of the 4 tubes per pixel using a straight section of 12-μm stainless-steel wire mounted to a fixture attached to an *XYZ* micrometer positioner. The size of epoxy was gauged by the wire diameter; the epoxy sphere diameter could be up to twice the wire diameter. The wire was inserted into the SU-8 tube and removed, leaving the top of the tube filled. We used vacuum tweezers attached to an *XYZ*-tilt stage to maneuver each absorber into position. Figure 6 shows the completed array. The pixels of the central 6×6 array have a 640 μm pitch, leaving about a 16 μm gap between the pixels. At the 4.5 m focal length of the X-ray mirror, each pixel subtends $29''$ and the full field of view is $2'.9$.

At the very corner of the 12 mm $\times$ 14 mm detector chip is a pair of additional devices nominally identical to those in the array, but located to be outside of the aperture. One of these is used in flight and is referred to as the calibration pixel. For in-flight gain calibration, a very small, collimated ^{55}Fe electron-capture source installed in the lid of the CTS that is pointed at the calibration pixel. When changes in gain are the result of drift in the heat-sink temperature, the gain history of a single pixel can be used to correct the gain of the entire array. The use of a collimated X-ray source and a dedicated calibration pixel makes it possible to achieve a low background at the main array by eliminating the electron-loss continuum that would be generated on the array if it were illuminated with a flood source. One JFET (corresponding to an edge pixel) was damaged during ground operations and so the finished instrument consisted of 30 array pixels and one calibration pixel.

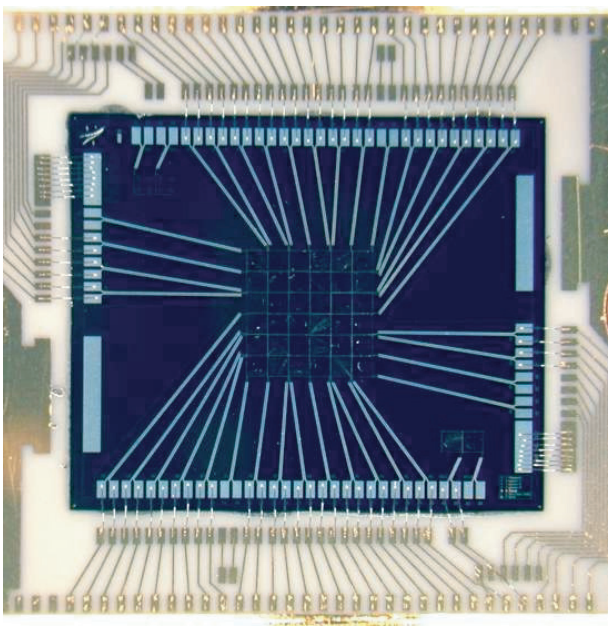

Fig. 6. Completed microcalorimeter array. The array consists of 36 pixels that are $624\,\mu\mathrm{m} \times 624\,\mu\mathrm{m}$. Of these, the four corner pixels are not read out for flight. One of the 32 electronics channels is further dedicated to the calibration pixel located on the bottom right, which is out of the telescope field of view. The typical gap size between the pixels is 16 μm, so the filling factor is about 95%.

3.2. *Performance and Characteristics of the Microcalorimeter Array*

On four arrays assembled, the resolution of the various pixels ranged from 5.3–6.5 eV FWHM, nearly independently of energy, except for typically 1–2 pixels per array. The resolution of those pixels for low-energy photons was similar to the rest of the pixels, but they degraded more rapidly with increasing energy. The characteristics of the flight array are summarized in tables 1 and 2. For flight operations, the detector system is biased to 2 V using the circuit shown in figure 9. This leads to the operating resistance given in table 1.

Despite the excellent performance, there were several unexpected features of the microcalorimeter array that became apparent in ground testing (see section 9). The ground testing allowed preparation for these effects in orbit, and preliminary indications from the limited in-orbit data indicate that the prepared procedures would have succeeded (section 10). The effects were differential gain changes, background events due to cosmic ray interaction in the thick frame of the device, and count-rate dependent noise.

The principle behind using a dedicated calibration pixel is that all pixels experience the same relative change in gain. It was expected that changes in the temperature of the warmer parts of the cryostat could, via conduction and radiation, change the temperature gradient between the control

Table 1. Detector parameters determined from fits of a representative pixel in the flight array at the operating temperature (~ 74 mK) under bias.

Parameter	Value
Heat capacity C of absorber (HgTe)	0.11–0.12 pJ K^{-1}
Thermal conductance G between absorber and thermistor	61 pW K^{-1}
Heat capacity C of thermistor	0.07 pJ K^{-1}
Thermal conductance G between thermistor and heat sink	60 pW K^{-1}
Resistance R at operating point	27.3 MΩ
$\alpha \equiv d\log R/d\log T$	-7.0
Effective time constant $\tau_{\rm eff}$ (for total C, G to heat sink, and α)	2.2 ms
Actual fall time (slowed by G between absorber and thermistor)	3.5 ms

Table 2. Absorption efficiency of the HgTe.

HgTe properties	Value
Mean areal density and 1σ deviation	$69.2 \pm 1\,\mu$g mm^{-2}
Theoretical 6 keV absorption efficiency	0.969 ± 0.0015
Nominal fraction of unit cell covered	$(0.624/0.640)^2 = 0.951$
Combined efficiency	0.92

thermometer and the actual detector heat sink or change the bolometric loading of the pixels, but that such effects would act on all pixels in the same way. What was found instead is that the calibration pixel responded more sensitively to changes in the neon and helium temperatures than did any pixel in the array, and that the outer pixels of the array were more sensitive than the inner pixels (subsection 9.1). A variety of possible causes were considered, but the pattern of sensitivity, with the calibration pixel being the most sensitive, invalidated most proposed mechanisms. One possibility still under consideration is differential absorbed power due to screening from surrounding pixels. The level of absorbed power is on the scale of tens of femto-watts; if it were uniform or constant it would have no impact on detector performance. Due to the differential sensitivity, however, gain correction based on the calibration pixel would overcorrect the gain of the pixels in the main array. We planned, in orbit, to make frequent use of the filter wheel position with calibration sources (see section 7 for details) in order to quantify the scale of the problem in normal operation (instead of just after cryogen transfers). Future calorimeter assemblies will be designed to reduce further the amount of long-wavelength radiation that can get into the detector enclosure.

We observed frequent groupings of nearly simultaneous pulses (time spans of hundreds of micro-seconds, based on time tags assigned by the CDP) on many pixels. We know from a variety of ground tests, including irradiation with alpha particles, that such events occur when an impulse of energy is deposited into the frame of the calorimeter chip and causes a pulse in the frame temperature. We will refer to the occurrence of such simultaneous pulses as a "frame event". Most frame events are low energy. A minimum ionizing particle going the shortest way through the frame deposits 150 keV into the silicon of the frame and makes pulses on multiple pixels that look like ~ 50 eV photons. Frame events amplify the apparent background rate because the area of the frame is 13 times the area of the biased pixels, and because each charged particle on the frame makes pulses on most of the pixels in the array. Because the cooling time for the frame turned out to be similar to the risetime for real X-ray events, the pulses produced in frame events are not easily distinguished from X-ray events based on pulse shape alone. Thus, rejection based on coincidence was required. Ground background data were analyzed in order to determine a screening algorithm based on the intervals between pulses, the number of pixels involved, and the pulse heights.

An effect related to frame events is count-rate dependent noise. When an X-ray is absorbed in the frame, the resulting frame-event pulses are too small to trigger, but they add to the noise of each pixel. Additionally, when a photon is absorbed in one pixel and that heat flows to the frame, a similar perturbation in the frame temperature occurs. This thermal crosstalk has been measured directly for gamma-rays, but for X-rays it just adds to the noise. These two terms combine to make the resolution depend on the photon flux and spectrum incident over the entire XRS aperture; the extra noise scales as $\Sigma_E \sqrt{N(E)E^2}$, where $N(E)$ is the number of photons at energy E. We determined a degradation function from ground calibration data, using data from inner pixels, outer pixels, and the calibration pixel in order to separate the effect of crosstalk from that of X-rays hitting the frame. In practice, this noise would have affected only observations of the brightest celestial sources; we anticipated that the resolution of the inner pixels would degrade to ~ 9 eV for an observation of a point source with a power-law spectrum with a flux of 10^{-8} erg s^{-1} cm^{-2} and unity photon index. In subsubsection 10.2.1 we show how this sensitivity affected the energy resolution in flight, due to the effects of cosmic-ray heat deposition in the Si frame of the array. Both the count-rate dependence of the resolution and the frame events can be reduced in future designs by improving the heat sinking of the array.

The XRS array had been mounted over a cut-out in an

alumina fan-out board using a fine line of Stycast 2850FT epoxy around the perimeter of the die. The thermal conductance of this link was measured for an equivalently mounted test array and was determined to be $90\,\mathrm{nW\,K^{-1}}$ at 60 mK. In later array designs, we have demonstrated that improved heat sinking can be achieved by depositing gold heat sinking pads on the array frame and connecting those regions to the detector thermal sink via gold wire bonds. On XRS, we chose to avoid the risk of adding an additional metal to the fabrication process, but we used gold to heat sink the alumina board, as described in subsection 3.5.

3.3. The Anticoincidence Detector

Because a fraction of cosmic rays that traverse the calorimeter pixels will leave behind energy comparable to photons in the XRS spectral bandwidth, an anticoincidence detector was implemented both to reject cosmic ray events and to be an independent monitor of the particle environment. We chose to employ a silicon ionization detector rather than another calorimeter in order to provide a faster signal with temperature invariant gain that could provide diagnostic information in the event of signal saturation on the calorimeter array. The XRS anticoincidence detector was designed to operate at the calorimeter heat sink temperature at low (< 9 V) bias so that it could be placed directly behind the calorimeter array. The sensor itself is a very simple design. The chip consists of $1\,\mathrm{cm^2} \times 0.5$ mm of high purity silicon (nominally 13–21 kΩ cm at room temperature). One surface is degenerately doped with phosphorus (n+) while the other is degenerately doped with boron (p+), and both sides are metalized with aluminum. Thus it is configured as a p-i-n diode and is operated with the standard reverse-bias relative to that configuration. The device should not be considered a diode at an operating temperature of ~ 60 mK, however, because the carriers in the central intrinsic region are completely frozen out and the detector is simply an insulator between metallic contacts. Biases up to 24 V were investigated. No change in gain was seen for biases above 2 V. The XRS anticoincidence detector was biased at 6 V using the circuit shown in figure 9. We patterned the contacts so that their edges were 0.15 mm from the physical edge of the chip, which was itself defined by DRIE. The corners of both the physical and the electrical perimeter were rounded. Thus we eliminated uncontrolled field-concentrating features and a possible breakdown path along dicing-induced surface states at the edge.

In flight operation, the pulse spectrum of the anticoincidence detector is not accumulated. Rather, the signal is compared to a commandable threshold, and if the signal exceeds that threshold during a time window associated with each calorimeter pulse, then the calorimeter signal is flagged. The energy equivalent of the 1σ value of the voltage noise was 1.6 keV. The default threshold was 16 keV, which was well below the 195 keV deposited by a minimum ionizing particle traversing the anticoincidence detector (0.5 mm of Si).

The calorimeter array was mounted on an alumina board that was placed directly on top of the anticoincidence detector board, with the anticoincidence detector itself fitting in a hole in the array board. The top surface of the particle detector sits 0.63 mm below the plane of the calorimeter pixels. Considering an isotropic flux of minimum-ionizing particles, 98% of those impacting the calorimeter array will pass through the anticoincidence detector. Those that miss the anticoincidence detector tend to have longer path lengths in the HgTe absorbers, enhancing their rejection based on their being out of the observational band. Using a GEANT[2] model, we determined that less than 0.1% of all incident minimum ionizing particles will deposit energy in the calorimeter of less than 10 keV without triggering the anticoincidence detector (Saab et al. 2004). An attempt was also made to model the unrejected background from secondary particles. The resulting prediction, though larger than that calculated for direct interaction of primary cosmic rays only, was less than that expected from scaling from the ASCA SIS background (Gendreau 1995), which was itself less than what was observed in orbit (see subsubsection 10.2.2). The underestimate is presumed due to the low-fidelity model used to describe the surrounding structure and from the failure to include all the relevant interactions in the simulation.

3.4. Microcalorimeter Front-End Detector Assembly (FEA)

The FEA contains most of the low temperature thermal and electrical support systems for the microcalorimeter array and anticoincidence detector. An overview of the FEA is shown in figures 7 and 8. The FEA was designed to make the microcalorimeter system modular and easily removable from the cryostat. This approach was adopted so that the FEA could be developed and tested in parallel with the ADR and He cryostat subsystems, and tested in different dewar systems prior to being integrated into the flight He insert. The FEA was also subjected to vibration tests as a subsystem. The CTS is suspended from the FEA housing using Kevlar™ cords and has a set of four annealed gold ribbons for connection to the thermal bus posts of the ADR (described in the next section).

The FEA also houses the first stage electrical read-out of the microcalorimeters and the anticoincidence detector. An overview of the first stage-read-out is shown in figure 9. The circuit is basically a JFET source-follower trans-impedance amplifier with nearly unit gain. The goal is to reduce the 30-MΩ source impedance of the microcalorimeter detectors (under bias) so that standard flexible cables can route the signals through the rest of the cryostat. The high source impedance forces the wiring between the detectors and the JFET's to be very taut to avoid microphonics. An additional complexity is that the JFET's are operated at 130 K to minimize their noise contribution to the read-out signal. The FEA thus contains nested thermal staging to keep the 130-K JFET's in close proximity to the 60-mK detectors while not contributing significantly to the parasitic heat load on the CTS and ADR. The JFET thermal staging must also not contribute significantly to the heat loads on the solid neon or helium cryogen tanks. This is described in more detail in subsection 3.6.

The fully assembled FEA is mounted over the magnet bore in the helium tank that contains the ADR and is bolted directly to the helium tank at 1.3 K. The top cover of the FEA contains the second of five infrared blocking filters (see section 6) completing the 1.3 K thermal shield for the CTS and the ADR.

[2] ⟨http://geant4.web.cern.ch/geant4/⟩.

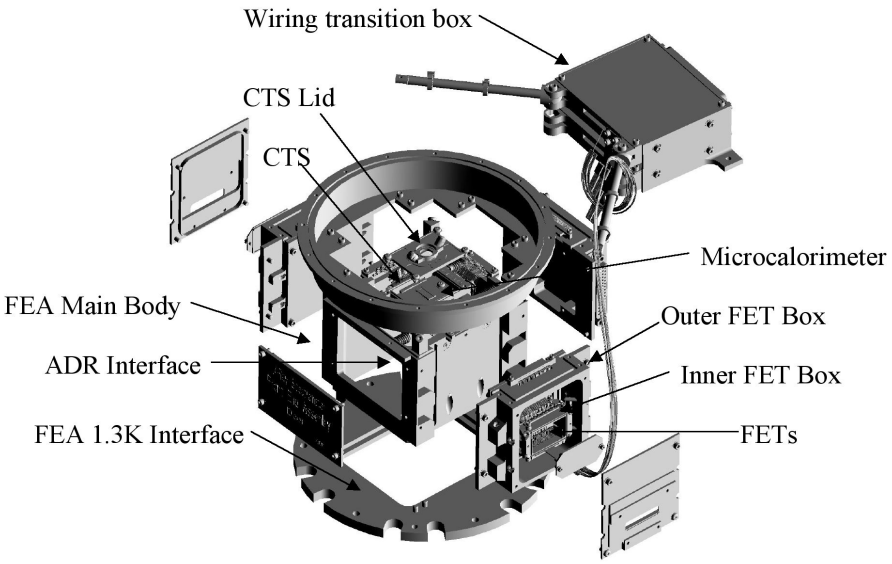

Fig. 7. Exploded view of the XRS Front End Assembly (FEA).

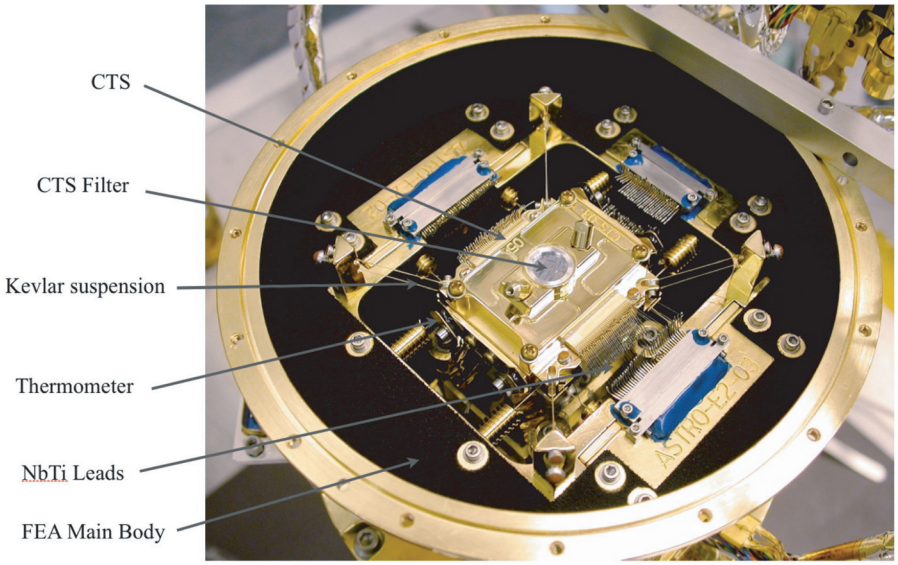

Fig. 8. Top view of the XRS FEA with its cover removed. The CTS is shown suspended in the center of the FEA main body.

3.5. The Calorimeter Thermal Sink

The Calorimeter Thermal Sink (CTS) is the temperature-controlled platform that houses the microcalorimeter array, an anticoincidence detector, and their associated load resistors. In addition, the CTS contains four RuO_2 thermistors that are the redundant control and monitor thermometers for the ADR. The temperature of the CTS is controlled at 60.0 mK with nominally $< 10\,\mu$K rms noise by regulating the external magnetic field applied to the salt pill.

The microcalorimeter array is housed inside the CTS with a tongue-and-groove lid to minimize stray light. The anticoincidence detector is mounted on an alumina fan-out board in contact with the bottom of the CTS. The calorimeter array is mounted over a cut-out in another high-purity alumina board that sits directly on the anticoincidence detector board. The two alumina boards are fastened to the CTS with a single screw-Belleville washer-flat washer combination. Available regions of the top and bottom surfaces of the calorimeter alumina board were plated with 4–5 μm of gold; top and bottom regions were connected via plated through holes. The top regions are connected to bosses in the CTS via ~ 40, 3-mm-long, 25-μm-diameter, gold wire bonds that in aggregate provide a 10-μW K^{-1} connection. Aluminum wire bonds connect the sensors to the fan-out boards and the fan-outs to the feedthroughs in the CTS. The electrical feedthroughs through

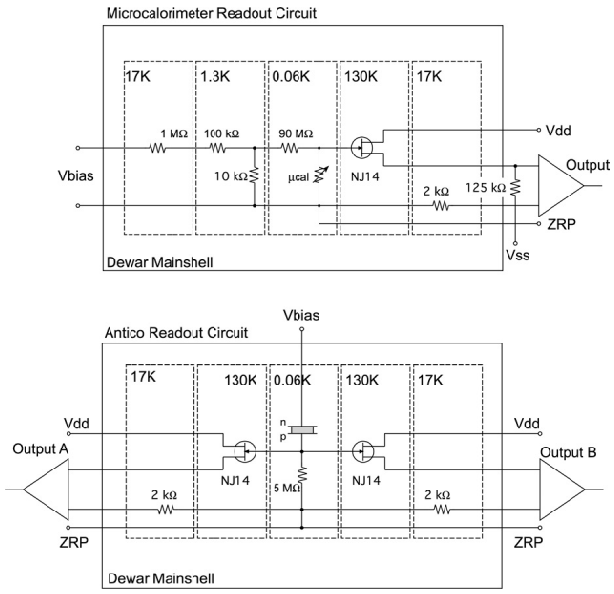

Fig. 9. A schematic diagram of the detector read out circuit. The top portion shows the bias and readout circuit for each of the microcalorimeter pixels. The ZRP ("Zero Reference Potential") refers to a set of 20 parallel conductors used to form a low impedance ($< 2\,\Omega$) reference to the CTS. The bottom portion illustrates the bias and readout circuit for the anticoincidence detector. The device is read out completely redundantly all the way out to and including the CAP electronics. The microcalorimeters and anticoincidence detector have independent bias circuits.

the wall of the CTS are custom-built alumina blocks which have a buried wire layer and are gold plated everywhere except for wire bond pads on the inside of the CTS and Be–Cu pins on the outside. The buried wiring layer contains two right angles so that there is no direct light path through the feedthroughs to the interior of the CTS.

The underside of the CTS contains an alumina board holding the 90-MΩ load resistors (see readout schematic in figure 9), which are located at 60 mK to minimize Johnson noise. The lid of the CTS contains one of the five aluminum-coated polyimide infrared blocking filters (section 6) and also a small, collimated ^{55}Fe calibration source. The isotope was deposited on a 2-μm-thick Ni foil and then attached to the end of a 100-μm-diameter Ni wire using Stycast 1266 epoxy. This was then epoxied into a stainless steel tube with a 127-μm-thick Be window epoxied in place using Scotchweld^{TM} 2216 epoxy. This hermetically sealed the source. The assembly was then epoxied into a longer stainless steel tube with a length of about 9 mm to provide the collimation. The source-end of that assembly was capped-off with another Be window. The source had an activity of 4.4 μCi (0.16 MBq) in 2003 August, and produced a counting rate of 6 counts s^{-1} on the calibration pixel when measured in 2003 December. The counting rate on the calibration pixel at launch was about 4 counts s^{-1}.

The thermal connection of the CTS to the ADR was made with four pairs of annealed, high-purity gold foils clamped to the CTS and to each of the four thermal posts of the salt pill. The gold-foil thermal connection to the salt pill was adopted to mechanically decouple the CTS from the ADR while permitting us to separately suspend the CTS to a higher resonance frequency. The thermal conductivity of the CTS to the ADR is $\sim 0.14\,\mathrm{mW\,K^{-1}}$ at 60 mK. This gives a ~ 1.7 mK drop to the salt pill thermal bus for the nominal 0.24 μW of parasitic heat input to the CTS.

The CTS is suspended from the outer housing of the FEA using 195 denier (1 denier = 1 g/9 km) Kevlar 49 tensioned to 1.18 kg. This gives the 70-g CTS a resonant frequency between 300 and 350 Hz (which was experimentally verified on an engineering model), making it safely isolated from the $\sim$90-Hz dewar resonance and the $\sim$200-Hz salt pill resonance. The Kevlar suspension contributes negligibly to the parasitic heat load on the ADR while providing a stiff support for the CTS. The CTS has maintained its alignment within the FEA to $< 25\,\mu$m throughout numerous thermal cycling and vibration tests.

The CTS is wired to both the JFET boxes (described in more detail below) and the bias box using 17-μm-diameter CuNi clad NbTi wire. The use of superconducting wire minimizes the parasitic heat flow from the 1.3-K connectors on the FEA to the 60-mK CTS. The superconducting wire is plated with a 0.8-μm layer of 70% Cu, 30% Ni alloy making the wire easily solderable using standard rosin fluxes. All of the wires bridging between the CTS and the FEA are tensioned across the gap between the two components by spring loaded Be–Cu contacts. The wires are tensioned to 6–10 g to raise the resonance frequency, and thus any associated microphonic signal, out of the detector bandpass (10–400 Hz). There are a total of 116 suspended and tensioned leads bridging the 1.3 K FEA housing to the CTS, dominating the 0.24 μW of parasitic heat load from the CTS to the ADR.

3.6. The JFET Trans-Impedance Amplifiers

The JFET stage itself presents a significant challenge in the design of a microcalorimeter instrument. While the detectors themselves must be run at very low temperatures, the JFET's must be operated at a significantly higher temperature in order to keep the carriers in the silicon from freezing out. For the XRS, the JFET's are thus temperature-controlled at 130 K. The JFET's must be located as close as possible to the array in order to minimize stray capacitance, which further complicates the design by requiring a high degree of thermal isolation, both conductive and radiative.

The JFET's used in the XRS are InterFET SNJ14AL16 that were supplied to us as bare dice. We then characterized the JFET's at 130 K, choosing the lowest noise components for assembly into the FEA. The noise performance of the JFET's in the flight assembly ranges from 3 to 5 nV Hz$^{-1/2}$ at 100 Hz. The JFET trans-impedance amplifiers convert the 30 MΩ source impedance of the detectors to the 1.8 kΩ output impedance of the JFET's, substantially reducing any microphonic contamination of the detector signal.

The XRS FEA contains two separate JFET assemblies to provide redundancy. The loss of one of the modular JFET assemblies allows half of the detectors to continue to function. The assemblies are mated through high-density connectors to the FEA main section where tensioned electrical leads make connection to the CTS. The JFET's are doubly suspended inside nested boxes. The outer box is bolted to the FEA body

and is thermally anchored at 1.3 K, while the inner box is thermally anchored to the neon tank at 17 K through a carefully routed thermal strap. The inner JFET box is suspended by 195-denier Kevlar inside the outer JFET box. Inside the inner JFET box, the JFET's themselves are organized into two separate packages of 9 JFET's each (16 for the microcalorimeters, 1 for the anticoincidence detector, and 1 spare). Each package also contains a diode thermometer and a heater for temperature control. The two packages are mounted on an aluminum substrate (totaling a few grams) that is then suspended with 55-denier Kevlar to the inner JFET box.

Light leaks from the 130-K JFET's were also a concern for the microcalorimeters and, to some extent, the ADR itself. To prevent long wavelength radiation from the JFET's from reaching the detectors, each JFET box has a specially constructed electrical feedthrough. The feedthroughs were fabricated using Eccosorb13 CR-117, iron-filled epoxy that provides effective shielding from the JFET's. There is no evidence for stray power on the microcalorimeter detectors that could be attributed to the JFET amplifiers. The JFET boxes do contribute $\sim 95\,\mu$W to the helium and 14 mW to the neon tank. Thus more than 99% of the power to run the JFET's is shunted away from the helium tank.

The wiring in both the inner and outer JFET boxes is 20 μm-diameter CuNi-clad stainless steel wire. The 1 μm 70% Cu, 30% Ni overcoat allows the wire to be soldered without using a highly corrosive flux. Stainless steel wire was chosen for its superior strength and low thermal conductivity. As on the CTS, the wiring in the JFET boxes is tensioned to avoid microphonics in the detector bandpass.

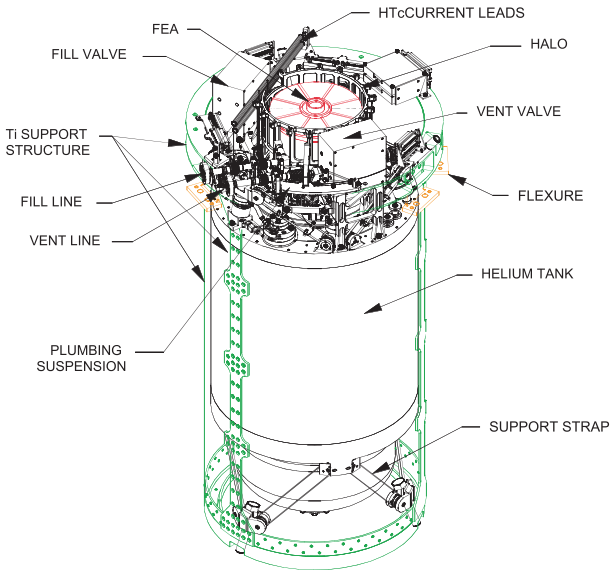

Fig. 10. Schematic of the XRS He Insert, consisting primarily of the He cryostat, ADR, and detector assembly. The Insert was designed to be modular and have simple interfaces to the Ne dewar. The titanium support structure is essentially a cylinder from which the He cryostat is suspended. The top-to-bottom length is about 79 cm and the dry mass is 42.3 kg.

4. Liquid He Cryostat

The He cryostat serves as the mechanical and thermal interface for the detector and ADR assembly. Design and performance details of the He cryostat have been presented over several years (Shirron et al. 2006; Breon et al. 2000; Volz et al. 1996). It was designed as a self-contained unit that is inserted into the Ne dewar with plumbing, electrical, mechanical, and thermal interfaces only at the front end. The interfaces are straightforward: fill and vent line connections, electrical connectors, and mounting flexures for structural support. This added to the complexity of the cryostat's front end layout and assembly, but ensured that all components critical to its performance were fully tested prior to integration with the Ne dewar.

Within mass and space allocations, the cryogen volume could not be much larger than about 30 liters, which translated to a maximum time averaged heat load of approximately 1 mW in order to meet the 3-year lifetime goal. This is roughly six times smaller than any previous superfluid helium dewar built for space, and required a far more careful assessment of heat loads. As a result, the XRS He cryostat pioneered several new technologies that enabled it, and future dewars, to meet such stringent cooling requirements.

The He Insert, shown in figure 10, consists of a 34.2 liter aluminum He tank supported inside a cylindrical titanium shell by 12 graphite/epoxy straps, the ADR and detector assembly, and valves, plumbing and phase separator to support the fill and vent operations. The magnet for the ADR is wound on an aluminum mandrel. This assembly is inserted into the front end of the He tank so that the magnet's windings are immersed in superfluid. The mounting flange on the mandrel makes an indium seal to the He tank. Heat from the ADR is absorbed either directly from the magnet's windings or the mounting flange. The fill and vent system has a specially designed porous plug phase separator that ensures 100% utilization of all venting helium (Shirron, DiPirro 1998) and the network of plumbing includes two heat exchangers along the vent line to provide maximum benefit from vapor cooling.

With such a complex and interdependent system, there are many potential design choices, and many trade studies were performed. Since many of these trades had to be completed before all dependencies were known, the final design is not necessarily fully optimized. Nevertheless, the design met the 3-year lifetime goal.

4.1. He Tank and Titanium Support Structure

The He tank is fabricated from aluminum cylindrical sections welded to machined aluminum heads. The He tank is contoured so that it and the 6 forward and 6 aft straps fit completely inside the titanium cylindrical shell that provides a uniform 17 K environment. The smallest gap between the He tank and shell is about 1 cm. Titanium is used for strength, so the entire He tank assembly can be cantilevered off the Ne tank using mounting flexures at the forward end. The straps are graphite/epoxy, and all are configured to provide both axial and tangential constraints on tank position. There are three attachment points on the He tank at each end (120° apart), and 3 on the shell at each end, offset from the He tank by 60°. Pairs of straps originate at each attachment point on the He tank and angle outward to the two closest attachment points on the

Ti shell (figure 10). This configuration achieves the required structural rigidity needed for launch on the M-V rocket with the lowest parasitic heat leak.

The straps at the forward end are shorter than those at the aft end, but have access to vapor cooling to intercept some of the extra heat local. The "warm" and "cold" heat exchangers in the vent line run at approximately 11 K and 3 K, under equilibrium flow conditions, and a system of copper wire heat straps thermally connects the 6 forward straps to these heat exchangers at optimal points along their length. Because of the distance and the difficulty of suspending straps along the He tank, vapor cooling the 6 aft straps would have had marginal benefit, and was therefore not done.

Radiative heat loads were minimized by coating and/or polishing the low temperature surfaces. Both the He and Ne tanks were highly polished, and the titanium shell was electroplated with gold. Radiative loads were not directly measured, but since they are one of the dominant heat sources, they could be estimated from measurements of the total load and knowledge of other individual loads. The estimates were consistent with the assumed emissivity of 0.05 for these surfaces.

4.2. Dewar Guard Vacuum

There is a single, shared vacuum space in the dewar that isolates the various temperature stages. The need to avoid even extremely small heat loads on the He Insert prompted the installation of a carbon/carbon composite getter on the He tank. Residual pressures as low as 10^{-8} torr would result in a heat leak of 25 μW from 17 K. The getter's surface area could accommodate 1.5 standard liters of helium gas at a pressure of less than 10^{-8} torr.

4.3. Fill and Vent Lines

The fill and vent lines and fluid control valves use a fairly standard configuration. Each line attaches to the He tank via a stepper-motor-controlled valve, and there is a similar valve located on the Ne tank that, when opened, allows helium to bypass the He tank. This is used for precooling the lines before a fill or topoff operation. The vent line also has a porous plug phase separator in parallel with its valve. The fill line is mechanically and thermally anchored to the vent line at the warm and cold heat exchangers. The penetrations to the He tank are located so the dewar can be filled and operated in both horizontal and vertical orientations, and such that the He tank can theoretically be filled to 97% (of 34.2 liters) when vertical, as it is in the launch tower.

The final topoff of the dewar before launch is performed with a supply dewar containing helium just above the superfluid transition, and the flight He tank pumped to $\sim$ 1.3 K. The goal is to end with the flight dewar as close to full as possible with helium as cold as possible. For three topoff procedures (a practice run and two pre-launch fills), all achieved 100% fill levels (of the maximum accessible volume of 33.1 liters) at 1.9–2.17 K. Lower temperatures were achieved when the transfer was terminated immediately on reaching 100%. In the best case, the final volume after continued pumping was 30.56 liters (92.3%) remaining after pumping down to 1.21 K.

4.4. Porous Plug Vent System

The phase separator used to retain liquid in the He tank while releasing boil-off vapor is based on "porous plugs" used successfully on previous space missions, but with modifications that prevent the loss of helium through film flow. Porous plug (PP) phase separators were first developed for the IRAS mission (Neugebauer et al. 1984), and use a plug of sintered stainless steel bonded into the vent line. The pores are typically a few μm in diameter, and stainless steel is used because of its low thermal conductivity. Under normal conditions, liquid in the He tank wets and fills the plug, and the lower pressure in the vent line causes evaporation on its upstream side. This sets up a temperature gradient which, in superfluid helium, also sets up a pressure gradient — known as the thermomechanical effect — which exceeds the difference in saturated vapor pressure on the two sides of the PP. The result is a net pressure acting to push liquid back through the PP into the He tank. This is usually balanced by surface tension, so that liquid is present on the upstream side of the PP and the temperature difference across it is on the order of a few mK.

In addition to the flow of helium through evaporation, there will be a flow of film from the perimeter of the PP. The flow is driven by van der Waals forces, and is constrained only by the superfluid critical velocity, v_c. For saturated films, v_c is inversely proportional to thickness, yielding the curious property that mass flow ($\rho_s\, v_c\, d$, where ρ_s is the superfluid density and d is the film thickness) is essentially constant, regardless of temperature and pressure. It is proportional to the portion of the vent line that has the smallest diameter, and is equivalent to a cooling loss of 1.24 mW per cm since the latent heat of the helium is not extracted from the remaining liquid. For typical sizes ($\sim$ 1 cm) this would exceed the total heat budget for the He dewar. A re-analysis of PP data from previous missions showed excess helium vent rates of exactly this magnitude, but it was not recognized at the time since the dewars had average heat loads of 100 mW or more. It should be noted that while the film's latent heat is lost, it does contribute to cooling. This can offset as much as 30% of the loss, but for the XRS this would still be catastrophic.

The solution was to use a relatively small porous plug and to thermally anchor a small diameter vent line to the He tank just upstream of the PP (Shirron, DiPirro 1998). The PP was sized to have a temperature drop of approximately 40–50 mK at the nominal flow rate of 40 μg s^{-1}. As the venting vapor and film exchange heat with the He tank, warming by 30–40 mK, the film is completely evaporated and heat is extracted from the He tank.

4.5. High-T_c Current Leads

A particular challenge for the XRS was the need for currents in the range of 0.5 to 2 A to run the stepper-motor valves and the ADR's magnet. Since both of these are mission critical and at times critical to safe operation, it was prudent to make their electrical leads fully redundant. With very limited vapor cooling available, normal metal leads could not be used to span the 17 K to 1.3 K gap, but using high-T_c superconductor leads posed the dual problem of fabricating leads sized for this current range and providing structural support for the

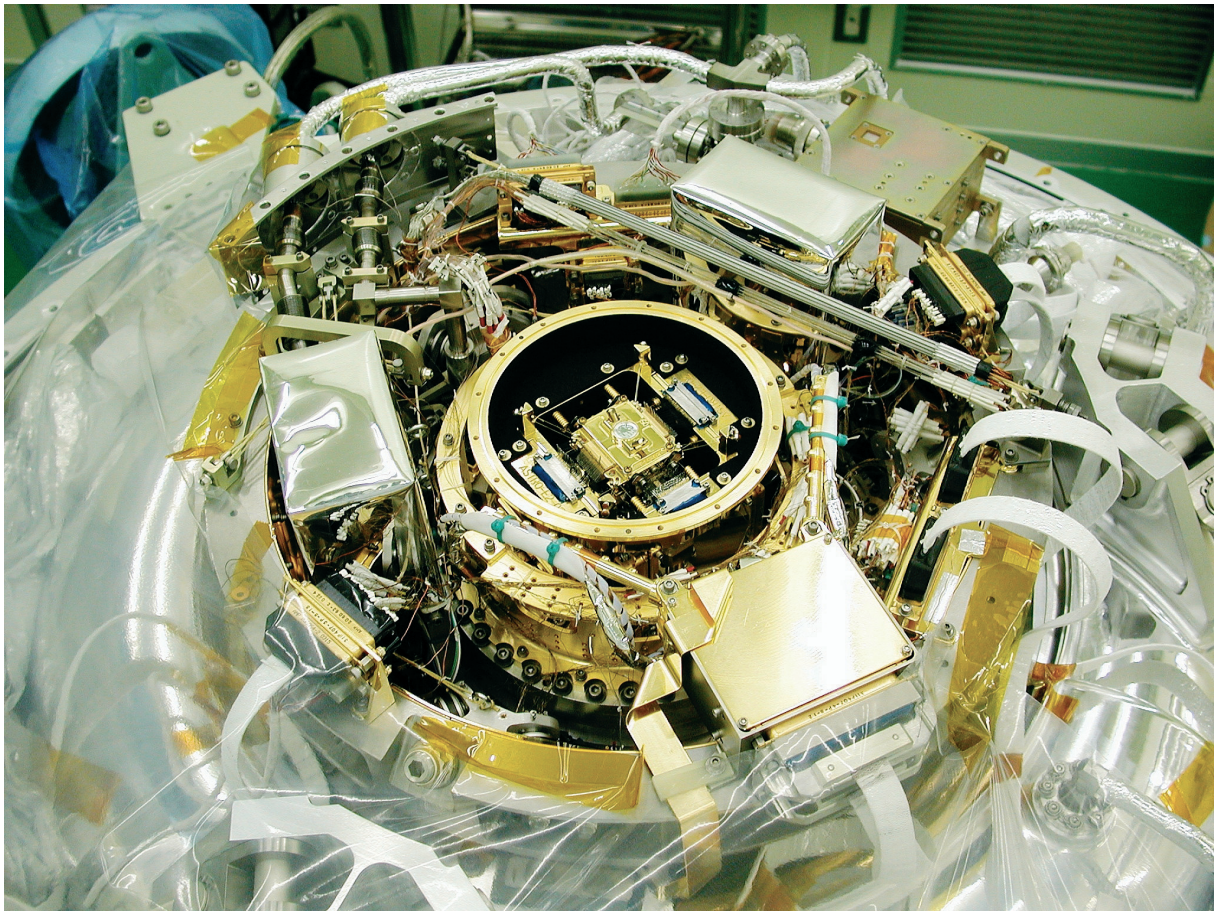

Fig. 11. The He Insert installed in the Ne dewar at SHI. The FEA is easily visible in the center. To the upper right and diagonally across the image are the high-T_c lead assemblies. The two shiny boxes at the top right and left are covers for the He cryo-valves. A similar such valve is mounted on the Ne tank and can be seen further to the top right. The box at the lower right is the transition connector box for the FEA. The top of the Ne tank is visible around the perimeter of the photo.

fragile leads without adding excessive thermal conductance. In the end, two different superconducting technologies and lead assemblies were adopted.

There are two high-T_c lead assemblies wired in parallel for redundancy. These can be seen in figure 11. The first assembly uses 12 YBCO filaments, each capable of carrying at least 10 A. The filaments are bonded to the outside of a thin tube formed from a sheet of fiberglass cloth impregnated with epoxy and supported by Kevlar rope strung along the center of the tube and attached to two G-10 washers bonded inside near the ends (Tuttle et al. 1998). In this way, the tube and filaments were not under any preload and needed to support only their own weight during accelerations. The filaments transitioned to niobium–titanium (NbTi) wires at the cold end, with the joint thermally anchored to the cold heat exchanger (at ~ 3 K). The heat conducted through the assembly from 17 K to the cold heat exchanger was 175 μW, and conduction to 1.3 K, through the NbTi wires, was negligible.

The second assembly uses 12 MgB_2 wires inside stainless steel tubing (Panek et al. 2004; Schlachter et al. 2006). To our knowledge, this is the first time this recently identified superconductor (Nagamatsu et al. 2001) has been used in space. The wires were bonded to the outside of two G-10 washers located roughly 1/3 of the way in from each end. This assembly was also supported by Kevlar rope attached to the G-10 washers, which were thermally anchored to the hot and cold heat exchangers on the vent line. The solder connections to NbTi wire at the cold end were anchored to the He tank. The conductance was significantly higher than for the YBCO set (435 μW to the cold heat exchanger and 34 μW to 1.3 K), but this unit was nonetheless adopted to provide an increased margin of safety against the leads being driven normal while carrying current in a situation where the heat exchanger temperature approached 8 K, which could potentially occur during some ground operations. Such conditions would likely cause the YBCO leads to become electrically open.

4.6. Adiabatic Demagnetization Refrigerator (ADR)

A single-stage ADR was used to physically support and cool the detector array to the operating temperature of 60 mK. The ADR consists of a 920-g ferric ammonium alum (FAA) "salt pill" in a 2-T NbTi magnet connected to the helium bath through an active gas-gap heat switch (GGHS). The switch uses a zeolite getter that, when cold, adsorbs the approximately 10 standard cm^3 of ^{3}He gas and opens the switch, and

when warmed above ~ 13 K releases enough gas to close the switch. The magnet was specially designed to produce 2 T with a current of just under 2 A. It has extensive shielding and bucking coils to zero out the dipole moment. This was both to limit the fringing field in the vicinity of the detectors and JFET amplifiers, and to minimize interference with spacecraft components such as magnetic torquers.

The heat switch directly connects the salt pill to an interface plate so that the assembly can be inserted into the magnet bore and thermally connected to the bath by bolting the plate to the magnet. The salt pill is thus physically cantilevered off the interface plate. This is accomplished by a suspension system consisting of a thin titanium shell (similar in function to the one surrounding the He tank) surrounding the salt pill, with end caps that support a network of Kevlar ropes that center the salt pill within the titanium shell. The end cap at the front end is fastened to the interface plate. The heat switch is a structural member in this assembly, mainly providing an axial constraint on the salt pill.

Cycling the ADR is accomplished by 1) ramping up the magnetic field, causing the salt pill to warm above the bath temperature, 2) closing the heat switch and continuing the ramp to full field, 3) waiting until the salt pill cools to 1.35 K and then opening the heat switch, and 4) ramping the magnetic field down to cool the detectors to 60 mK. In step 2, the ramp rate is regulated to keep the salt pill from warming above 1.8 K. This was done to minimize the total amount of heat transferred to the helium bath, which comes from three main sources: hysteresis heat from the magnet, heat used to warm the getter to activate the heat switch, and heat from the salt pill. Magnet hysteresis heat depends only on the field excursion, not on the rate or duration. Heat from the getter depends on the amount of time the switch is closed, so more aggressive magnetization rates will reduce the total. However, the heat generated by the salt pill is proportional to its temperature during magnetization, and this favors less aggressive rates.

4.7. He Cryostat Qualification

Any helium leak into the guard vacuum that is detectable at room temperature would certainly present problems for the helium dewar when filled with liquid cryogen. As such, the He cryostat was tested for leaks on numerous occasions using ^{4}He. It was also tested for ^{3}He that could be a sign of the exchange gas leaking from the gas-gap heat switch. A data logger and differential techniques were used to achieve very high sensitivity. The leak rate sensitivity was typically better than 1×10^{-10} std. cm^3 s^{-1}; on one occasion a leak rate of 1×10^{-11} std. cm^3 s^{-1} was discovered and pinpointed using exhaustive measures to establish an extremely low He background in the laboratory. No leaks were found in the cryostat, warm or cold, to better than 1×10^{-10} std. cm^3 s^{-1}.

The ^{3}He leak rate requirement is based on operation of the heat switch. Note also that the higher room temperature reading drops dramatically when a surface with a temperature capable of condensing a film of ^{3}He, such as a tank of liquid ^{4}He, is present. No liquid He was present during this leak test of the ^{3}He switch. The ^{3}He signal was less than 6×10^{-8} std. cm^3 s^{-1} at room temperature and 4×10^{-9} std. cm^3 s^{-1} at 60 K.

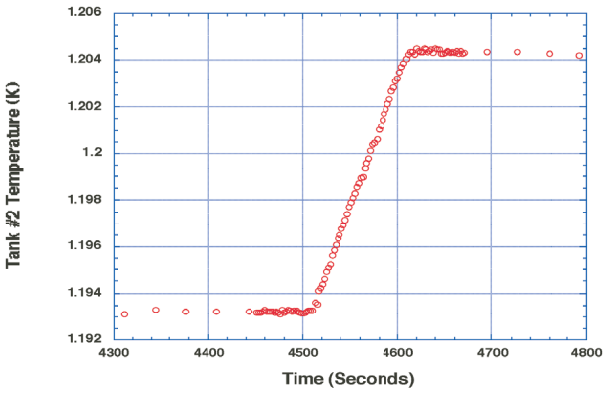

Fig. 12. Response of the He tank to a mass gauge measurement. For this test, the inferred volume was 15.6 liters, while the result from a liquid level meter mounted in the cryostat for ground servicing was within 5% of this value. This accuracy was verified on several occasions.

The two Astro-E2 XRS cold valves operated properly both at 4.2 K and superfluid temperatures. The valve seat leak requirement is based on direct loss of liquid. The vent valve leak rate cannot be verified directly since it is in parallel with the porous plug and heat exchanger. It was verified to be closed indirectly through the parasitic heat measurements described in the next subsection. The fill valve when closed is leak tight to at least 1.6×10^{-6} std. cm^3 s^{-1} ($< 1 \times 10^{-4}$ std. cm^3 s^{-1} required).

The XRS has a He mass gauge system that consists of a heater and several redundant thermometers mounted within the He tank. A pulse of heat is added and the temperature is monitored. One of these thermometers is read out repeatedly by the ACHE for the duration of the mass gauging, including a minute before and after the heat is added to evaluate the pre- and post-pulse trends versus time. The procedure is to apply a constant current of 4.88 mA for 100 s to a resistor mounted in the tank with a resistance of 3746 Ω. This gives a heat pulse of 8.92 J. The response to a mass gauge measurement made during ground testing is shown in figure 12. The temperature-versus-time slopes are then extrapolated to the middle of the heat pulse profile. The difference in temperatures is used to determine the heat capacity of the system, which is dominated at all fill levels by the liquid helium. Knowledge of the specific heat of liquid and gaseous helium (more precisely, internal energy) is used to calculate the remaining mass of the liquid from the temperature difference (DiPirro et al. 1994).

The porous plug and heat exchanger assembly was tested with the cold vent valve closed and with the test dewar tilted to 70° in order to wet the porous plug with superfluid. The flow rate through the porous plug was varied by throttling external valves. The temperature of the porous plug and the flow rates as measured on a Hastings mass flow meter were recorded at several points of decreasing flow rate. Results of these tests are shown in figure 13.

In addition, during the parasitic heat load test (see next section), the equilibrium temperature of the He tank was lowered from 1.3 K to 1.23 K. This resulted in a lower parasitic load, which can be completely explained by the earlier porous plug and heat exchanger tests. These results confirm that no

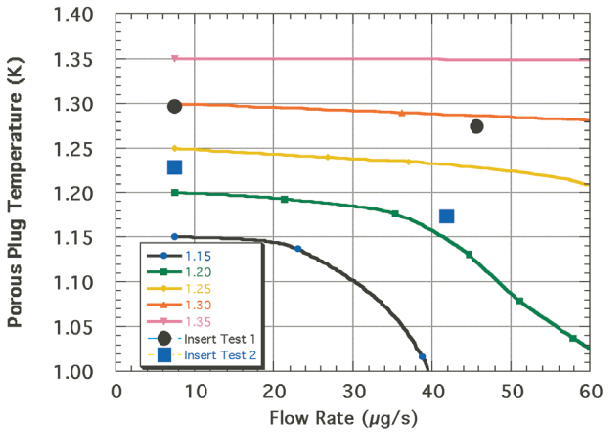

Fig. 13. Comparison of component test of porous plug assembly (lines) with tests in Insert (large circles and squares). The component tests were performed with simulated tank temperatures ranging from 1.15 K to 1.35 K. It is seen that the He Insert test results, which were done at slightly different temperatures than the component tests, are consistent with the curves of the component tests.

Table 3. Break-down of the parasitic heat load to the He tank.

Heat source	Model value [μW]
Radiation	138
Forward support straps	225
Aft support straps	196
JFET's	95
HTS leads for magnet and valves	83
All other wiring	73
Plumbing	54
Kevlar supports	16
Total	880

excess superfluid film gets past the heat exchanger. Eddy currents generated by ramping the magnet produce negligible heating in the ADR or in the He tank.

4.8. *He Cryostat Heat Loads*

The cryostat parasitic heat loads (JFET's on, but no ADR operation) under the boundary condition of a 17 K Ne tank temperature were measured. The result of 903 μW is close to the 880 μW predicted by the model (table 3). This compares with 711 μW for Astro-E XRS with a similar boundary condition. The difference appears to be mainly due to the higher conductance of the MgB_2 leads than the redundant YBCO leads of Astro-E XRS (75%) and the support strap heat sink locations (15%), with the remainder of unidentified origin.

The heat flow is measured by volume flow rate of helium gas pumped out of the cryostat vent line and through a Hastings mass flow meter and a wet test meter in series. The volume flow rate is converted to mass flow rate using temperature and pressure corrections and the ideal gas law. The temperature of the He tank is required to be extremely stable during these tests ($< 0.25\,\mathrm{mK\,h^{-1}}$ required with a goal of $< 0.1\,\mathrm{mK\,h^{-1}}$) so that only small corrections due to the net heat flow into or out of the liquid need to be made. In our final measurements we achieved drift rates of 0.02 and $0.06\,\mathrm{mK\,h^{-1}}$ with a result that less than 10 μW is attributable to this net heat.

In addition, the effects of the porous plug temperature drop and heat exchanger effectiveness were determined by changing the operating temperature of the He tank. The $903 \pm 20\,\mu$W (the error bar is due to accuracy rather than precision of the measurement) was measured with the He tank at 1.228 K and the porous plug at 1.172 K. When measured with the He tank at 1.297 K and the porous plug at 1.275 K, the parasitic heat was 996 μW. The difference is due to the small amount of film flow leakage when the temperature difference across the porous plug and heat exchanger is less than 40 mK. Note that to calculate the heat of vaporization, and hence the heat load in microwatts and the lifetime in years, the temperature used is the He tank temperature and not the porous plug exit temperature. This is because the heat exchanger not only evaporates the residual superfluid film at the He tank temperature, but also thermalizes the boil-off gas, thus recovering the higher heat of vaporization of the He tank temperature. For example, the latent heat of vaporization at 1.228 K is $21.51\,\mathrm{J\,g^{-1}}$. At 1.172 K it is $21.26\,\mathrm{J\,g^{-1}}$. However, the change in enthalpy of the gas going from the porous plug temperature of 1.172 K to the heat exchanger at 1.228 K is $0.27\,\mathrm{J\,g^{-1}}$, more than making up for the difference. For simplicity, the calculations only use the latent heat of liquid helium at the tank temperature.

4.9. *ADR Performance*

From an operational perspective, we distinguish two separate parts to the ADR cycle: cycling the ADR to cool the salt pill to 60 mK (Gross Cycle Control, or GCC) and regulating the magnet current to maintain 60 mK (Tight Temperature Control, or TTC).

When the ACHE receives the GCC execution command, it initializes the software, enables limit checking, verifies that all the temperatures are within the safe limits, and then switches to current control mode. The ACHE ramps up the magnet current at 31 mA per step in a specified time interval (default is 16 s). During this process, the salt pill heats up due to magnetization. When the salt pill reaches 0.85 K, the heat switch getter circuit is turned on. Within about a minute or so the heat switch is thermally closed, and thermally connects the salt pill to the helium bath. (The getter temperature reaches a maximum of about 14 K.) The current continues to increase until a maximum of 2 A is reached. At this point, the ACHE limits the temperature of the salt pill to less than 1.8 K, but it typically only reaches 1.6 K during this time. Eventually, the salt pill begins to cool and the getter heater is turned off when the salt pill falls to 1.35 K. Once the getter cools to 11 K, the current is then ramped down at 53.3 mA per step until the current is at 0.5 A. This procedure is repeated at a reduced rate of 13.1 mA per step until the current is 0.125 A. The ACHE now continues at this ramp down rate and monitors the control thermometer located on the CTS and switches to TTC once a temperature, sampled three times, below the target value of 60 mK is recorded. The remaining current being supplied to the magnet is typically 50 mA, and this is regulated to maintain a temperature of 60 mK until the cooling power is depleted at

zero current. At that point a new GCC command is issued, or earlier, depending on optimizing spacecraft operations.

For operation at 60 mK, FAA has the highest cooling capacity of common ADR refrigerants. The 2 T field achieves optimal entropy suppression of approximately 50% at the bath temperature, and yields a cooling capacity of 0.42 J at 60 mK. This will support a heat load of 4.9 μW for the required 24 hour hold time. The combined parasitic heat leak from the heat switch, the Kevlar suspension and the CTS wiring is $\sim 5.0\,\mu$W. Consequently, the ADR is expected to hold 60 mK for just under 24 hours for a nominal He bath temperature of 1.3 K. As will be described later, the He bath cooled to below 1.2 K in orbit, and consequently the ADR hold time significantly exceeded the requirement.

The ADR hold time under TTC was measured during ground testing for two cycles when the He tank temperature was held at approximately 1.3 K. The hold times at 60 mK were 25.7 hours and 26.7 hours, respectively, exceeding the minimum required hold time of 24 hours. This is consistent with the separately determined heat load on the salt pill of $\sim 5.0\,\mu$W, due mainly to heat conducted through the shell of the heat switch, and, to a much lower extent, heat from the CTS wiring to the FEA housing.

On orbit, the expected He tank temperature was 1.21 K. At this lower temperature the current at the start of TTC should be larger and the parasitic heat load on the ADR smaller, both tending to increase the hold time. Based on ground measurements, the estimated effect on hold time goes as $T(\mathrm{He})^{-3.6}$. Using this extrapolation, it was estimated that the hold time on orbit would be 33.7 hours. This can be compared with the inferred in-flight performance of 38 hours given in table 10 (p. S105). The heat dumped per GCC and the duration of the GCC was expected to be approximately the same, so the average heat load to the He tank from the ADR on orbit was predicted to be $179 \pm 20\,\mu$W. The larger error is due to the uncertainty in the extrapolation.

The ADR heat load on the He tank was measured on the second and third GCC's after the He bath was stabilized at 1.3 K. The heat load was measured calorimetrically during ground testing by measuring the temperature change on the liquid helium in the He tank. Combined with a knowledge of the specific heat of liquid helium, the amount of liquid in the He tank and the total volume of the He tank, the heat dumped was 22.3 J on the second GCC and 22.5 J on the third GCC. This compares with 20.7 J measured for Astro-E XRS obtained during ground tests. The first GCC was not used in the analysis because it was done from a starting ADR temperature of ~ 1.3 K, which would result in a greater heat load to the bath and is not the normal mode of operation. The second and third GCCs took 64 minutes to completely execute (transition to TTC). The last part of the heating, as indicated in figure 14, is due entirely to magnet hysteresis. We find 4.5 J dumped in this part of the cycle alone. Since the hysteresis heating is symmetric, we expect a total magnet dissipation of 9.0 J per cycle. This compares with 6.4 J measured for the Astro-E XRS magnet. This alone more than covers the difference in heat dumped between the Astro-E and Astro-E2 XRS ADR's.

Combining the GCC time with the TTC duration and dividing the total into the average heat load gives an average power into the cryostat from the ADR of $228 \pm 5\,\mu$W for a He temperature of 1.3 K.

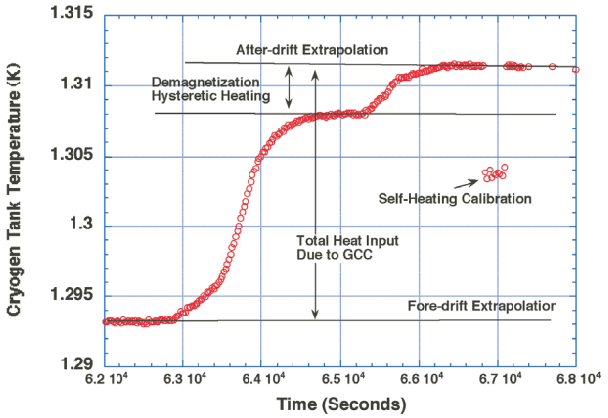

Fig. 14. Calorimetric measurement of the ADR heat load on the He tank during Gross Cycle Control.

4.10. Expected On-Orbit Lifetime

The thermal model we developed to predict the lifetime (Breon et al. 2000) shows that there is significantly reduced parasitic heat input to the He cryostat due to increased vapor cooling. It is therefore important to use the model to combine the measured parasitic heat into the He tank with the heat dissipated in the He tank by the ADR on a periodic basis. Note that while the ADR heat is dumped to the He tank over only $\sim 3\%$ of the cycle, for the majority of the mission the large heat capacity of the helium and the low flow rate result in a very long time constant — on the order of two weeks. It is therefore allowable to use a constant extra heat from the ADR.

First the results for the benchmark boundary temperatures of 17 K at the Ne interface and 1.3 K at the He tank are calculated. To force the model to give the measured 903 μW instead of the 880 μW predicted, 35 μW is added directly to the He tank. Then the 228 μW from the ADR is added. The result is $1059 \pm 41\,\mu$W. If we assume a 90% fill (out of a nominal 33.1 liter volume) at launch, the heat load leads to a lifetime of 2.79 ± 0.11 yr.

If we then use the expected boundary conditions of 16.24 K at the Ne tank, and 1.21 K at the He tank, the total heat load is calculated to be $952 \pm 69\,\mu$W resulting in a lifetime of 3.01 ± 0.22 yr starting from 90% full at launch. The 16.24 K value for the Ne tank is the highest of three temperatures measured on the engineering model (EM) dewar Ne tank for Astro-E XRS. It is also conservative in that the EM Ne tank has a known higher heat load than the flight Ne tank, and that the heat load was higher due to 300 K ambient temperature on the outer shell rather than the < 250 K expected on orbit. The 1.21 K He tank temperature is derived from impedance measurements on the EM dewar helium vent plumbing and the porous plug measurements made from Astro-E2 XRS.

Table 4. Requirements for the Ne dewar.

Neon temperature	< 17 K
Neon lifetime	> 2 yr (goal: > 3 yr)
Amount of solid neon	> 120 L
Main shell temperature	< 230 K

5. Ne Dewar

The Ne dewar of the XRS is a vacuum-insulated vessel that provides a 17 K enclosure to the He Insert using solid neon and maintains the cryogenic environment during ground testing, launch, and in orbit (Fujimoto et al. 2006). The ultimate design requirement (goal) for the Ne dewar is to achieve a lifetime of 2 years (3 years) in orbit, under various constraints at launch and in orbit. In this section, we describe the design of the Ne dewar and its performance.

5.1. Requirements and Design Concept

A preliminary design of the Ne dewar was performed in 1994 (Volz et al. 1996). To keep ~ 30 liter superfluid liquid helium for more than 3 years, the total heat load to the He tank must be smaller than 1 mW. We adopted 120 liters of solid neon as the second cryogen, which provides 17 K enclosure to the He Insert (table 4).

As with the He cryostat, the design challenge of the Ne dewar was to achieve 2–3 year lifetime of solid neon in orbit and to sustain against the mechanical environment during the launch. Since Suzaku is in a low-Earth orbit, with the altitude of about 568 km, and performs pointing observations, there is a considerable heat input from the earth. Moreover, the vibration and the shock levels during the launch of M-V rocket are also very severe. To mitigate the shock level on the dewar, the Ne dewar mounting has shock absorbers and support straps optimized to satisfy these conflicting requirements.

5.2. Design of the Ne Dewar

Figures 15 and 16 show a side view and cross sections of the Ne dewar, respectively, while figure 17 shows a schematic view of the plumbing. As shown in these figures, the Ne dewar is composed of a 120 liter toroidal tank, a main shell, three vapor-cooled shields (VCS), multi-layer insulation (MLI), plumbing to the He and Ne tanks, valves, an aperture for X-rays, and mechanical structures to support these components, i.e., support straps and shock absorbers. A single-stage Stirling-cycle mechanical cooler is installed at the dewar girth ring, which is described in subsection 5.3. The total dry weight of the dewar including the He Insert and the mechanical cooler is 223.26 kg, and design values of the initial mass of the solid neon and liquid helium are 172.8 kg and 4.3 kg, respectively, bringing the total weight at launch to 400 kg.

The Ne tank is machined from aluminum alloy as two shells with 2-mm wall thickness. The shells are then filled with an aluminum foam and joined. The foam works as a heat exchanger and keeps the neon temperature uniform. At the inner surface of the toroidal tank, there is an interface flange to the He Insert, called the 17-K interface. This interface is where the flexures of the He Insert are attached. The top and bottom

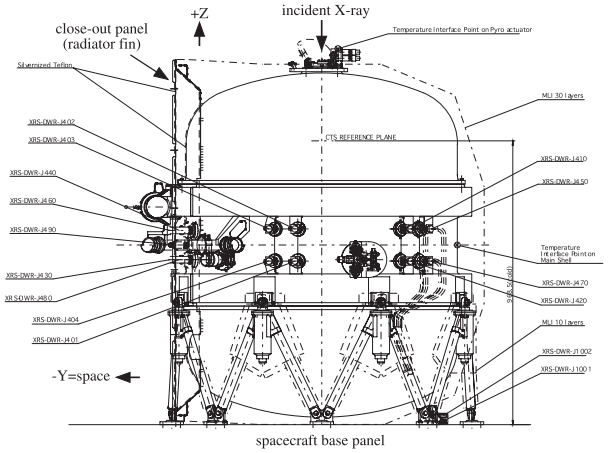

Fig. 15. Side view of the Ne dewar.

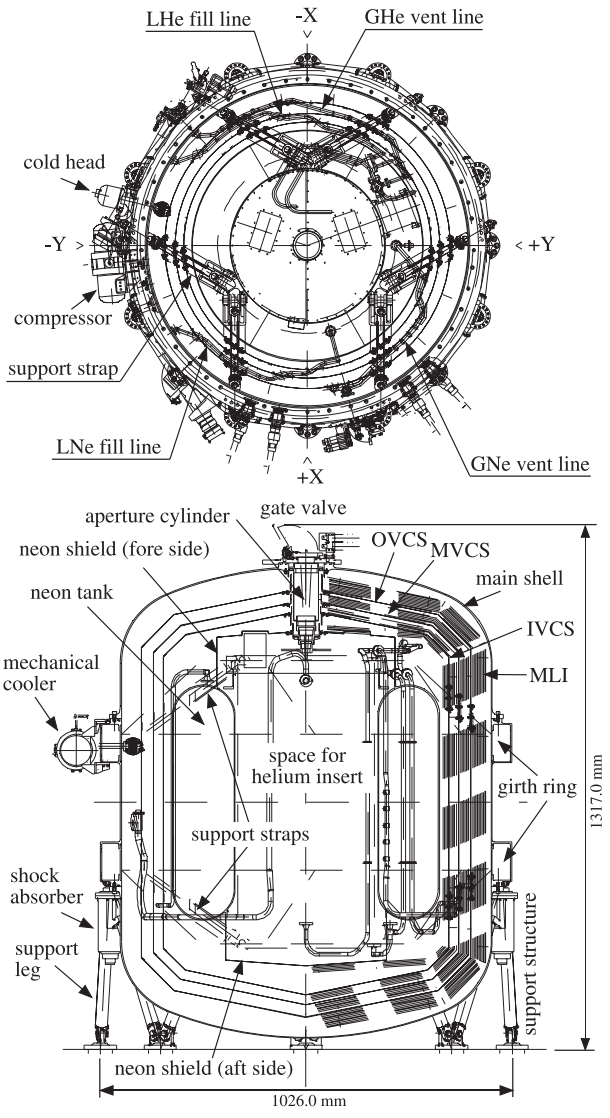

Fig. 16. Cross sections of the Ne dewar. The radiator close-out panel is not shown in this drawing.

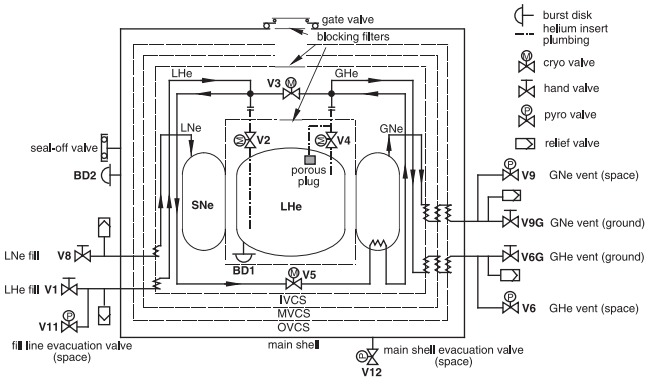

Fig. 17. Schematic view of the plumbing and valves inside the Ne dewar.

ends of the Ne tank are closed out with shrouds connected to the Ne tank. Once the tank is filled with solid neon, all of the Ne tank valves are closed until launch. On the ground, it is regularly cooled down by flowing liquid helium around the Ne tank through valve V5 shown in figure 17, so that the neon temperature is kept below its melting point (24 K). Soon after launch, the Ne vent valve (V9) is opened, and pumping down starts. This keeps the neon temperature below 17 K.

The Ne tank is supported by 12 straps connected to the main shell (figure 16). A significant fraction of the incoming heat to the Ne tank is from thermal conduction through these support straps. Therefore, it is crucial to make the thermal conductance of the straps as small as possible while keeping the strength to withstand the mechanical environment at launch. To meet these requirements, we adopted S2-GFRP (glass fiber reinforced plastic) belts as straps and titanium alloy as joints. We also implemented shock absorbers using Belleville springs at the joints of the main shell and the support legs. These mitigate shock to the Ne tank during launch by about 20%. As a result, straps with a cross section of 16.6 mm $\times$ 1 mm were adopted, which is fatigue-limited against cyclic stress, and the fraction of the heat load to the Ne tank attributed to the support straps was reduced to about 25% (see also figure 39 in subsection 10.1).

Thermal insulation is achieved by the main shell, VCS, and MLI. The main shell is the outermost container made of 3.0–3.5 mm thick aluminum alloy. Its height and diameter are 1184.5 mm and 926 mm, respectively. Part of the main shell surface is exposed to space, and works as a radiator. This area is coated with silver Teflon tape. The unexposed part of the dewar surface, which is interior to the spacecraft, is covered with MLI, 10 layers around the support structure and 30 layers for other parts. A radiator close-out panel is attached to the main shell, which fills the gap between the dewar and the spacecraft (figure 15). Using these radiators, the main shell surface temperature is kept at about 230 K when the mechanical cooler is off, and at 250 K when the mechanical cooler is operating with full power. Between the main shell and the Ne tank, there are three vapor-cooled shields, inner (IVCS), middle (MVCS), and outer (OVCS), which are cooled by sublimed neon and evaporated helium. These shields are made of 0.4 mm thick aluminum alloy. There are MLI blankets between the main shell and the OVCS (50 layers), OVCS and MVCS (30 layers), MVCS and IVCS (20 layers), and IVCS and the Ne tank (20 layers). The VCS's and MLI reduce incident radiation from the main shell to the Ne tank.

In addition to the manual and electromechanical cryo-valves for ground operations, there are five pyro-valves for: venting helium (V6), venting neon (V9), evacuating the helium fill-line (V11), evacuating the guard vacuum (V12), and the X-ray aperture (gate valve). All these valves are opened with pyro-cutters after launch. At the center of the gate valve of the Astro-E2 XRS, there is a beryllium window with 100-μm thickness and 5-mm radius. This allows performance verification of the detector on the ground and during the initial phase in orbit using an ^{55}Fe radioisotope source, without opening the gate valve.

There are 7 flight and 7 GSE temperature sensors in the dewar,[3] three ruthenium-oxide sensors for the Ne tank, and one platinum sensor for IVCS, MVCS, OVCS, and the main shell, respectively. These sensors are activated and measured by the ACHE. Cables made of twisted pair manganin wire were used for the temperature sensors and the electromechanical cryo-valves in the dewar. Custom-made flat cables were used for the calorimeter sensor channels and some temperature sensors inside the He Insert. The magnet lead is a twisted pair made of oxygen-free copper, and is laid down inside the plumbing for venting neon gas.

5.3. *Mechanical Cooler*

For the original Astro-E program, we fabricated two dewars, an engineering model (EM) and a flight model (FM), and verified the thermal performance. The measured heat load from the Ne tank to the He tank was 629 μW (without the ADR heat loading), which was well below the requirement. Hence, the lifetime of the Astro-E XRS in orbit would have been limited by the amount of solid neon to 1.95 years. We therefore extensively investigated the possibility of extending the lifetime of solid neon with minimum risks. A solution that we identified was to cool down the OVCS with a mechanical cooler from 195 K of Astro-E to 135–100 K, where the range depends on the mechanical cooler operational duty cycle (50–100%). The resulting expected lifetime would be increased to 2.4–3.5 years, and a lifetime of 1.92 years could be achieved even if the mechanical cooler were to fail or were otherwise not operated on-orbit. Microphonics was a concern from the viewpoint of the detector performance. However, since the observing efficiency of Suzaku is typically 40–50% due to Earth occultation and the SAA (South Atlantic Anomaly), we had the option to reduce the power or not to operate during observations. Therefore, we concluded that there was virtually no risk to installing the mechanical cooler on the Astro-E2 XRS dewar.

The mechanical cooler adopted for the Astro-E2 XRS (table 5) is a single-stage Stirling-cycle cooler developed by SHI (Narasaki et al. 2006). Both the cold head and the compressor are mounted on the surface of the dewar girth ring (see figures 15 and 16). The compressor is in a face-face-type

[3] This number does not include the sensors inside the He Insert and for the X-ray filters.

Table 5. Specifications of the mechanical cooler adopted for the Astro-E2 XRS dewar.

Cooling power	2.4 W/100 K (BOL), 2.0 W/100 K (EOL)
Power consumption	0–35 W
Drive frequency	52 ± 1 Hz with 0.1 Hz step
Life time	> 3 yr
Weight	4.2 kg (cold head + compressor)

Fig. 18. Finished XRS dewar prior to spacecraft iteration. The rectangular frame attached to the dewar is the radiator close-out panel which fills the gap between the dewar and the spacecraft. The mechanical cooler cold head and compressor are mounted to the upper girth ring.

configuration, and, by adjusting the mass balance, vibrations can be significantly reduced. The mechanical cooler is driven by the XRS-CDE (Cooler Drive Electronics), with a commanded voltage. The cooler drive frequency is adjustable in a ± 1 Hz band around 52 Hz with a step size of 0.1 Hz. The maximum power of the cooler is 35 W, with an initial cooling power of 2.4 W at 100 K. The drive circuit is grounded at the CDE. The vibration level at the girth ring due to the mechanical cooler was about 10 mG rms. Its impact on the detector performance was measured after the dewar fabrication was completed, and is described in subsection 9.2.

5.4. Fabrication and Ground Operations

Fabrication of the Ne dewar for the Astro-E2 XRS started at SHI in 2001. The He Insert, assembled at Goddard, was integrated into the dewar in 2004 March, and, after closing out the forward thermal shields and blanketing, assembly of the dewar was completed in 2004 June. The dewar was then pumped down to about 1 torr in a very controlled fashion (constant $P/\dot{P}$) in order to keep the pressure gradients across the blocking filters from changing, and then pumped at maximum speed for about 1 month. The dewar was then filled with cryogens, first with liquid neon (to about 10%) and then filled with liquid helium and pumped to about 1.3 K. After this, the dewar was functionally tested and characterized with external X-ray sources for about 3 weeks (discussed in section 9) before being shipped to ISAS/JAXA for vibration and shock tests, and integration on to the spacecraft. In 2004 September, the Ne tank was filled to 100% with liquid neon, which was then frozen solid by flowing liquid helium around the Ne tank. The total mass of solid neon filling the tank was 173.24 kg. The dewar was then attached to the spacecraft.

During the ground test phase of the spacecraft, the solid neon was cooled down approximately once per three weeks, and was kept at 13–21 K. In addition, a liquid level sensor was used as a heater to boil off He and increase the vapor cooling to the IVCS. This was done to maintain a suitably low temperature (below 140 K) to prevent water vapor migration to colder parts of the dewar (in particular, the Ne filter). This operation was repeated almost every day until launch.

6. Dewar Aperture and Blocking Filters

The Aperture Assembly supports four of the blocking filter mounts and their associated blocking filters. The blocking filters are required to isolate the microcalorimeter array from radiation from the ambient temperature of the spacecraft and internal thermal stages. There are three sub-assemblies: the aperture cylinder, the neon filter mount, and the FEA filter mount. The assembly is designed to support the filters within the optical path at the following design temperatures: Dewar Main Shell (DMS, 230–240 K), IVCS (86–126 K), Neon (17 K), and FEA (1.3 K). A secondary requirement of the filter mounts is to prevent the flow of water vapor onto the (cold) filters via a nested set of baffles. The Aperture Cylinder, which holds the DMS filter at one end and the IVCS filter mount at the other, is attached at the dewar at the main shell. The IVCS end of the cylinder is cantilevered with a thermal strap connecting it to the IVCS. The Neon Filter Mount is attached to the top of the dewar's Neon shield and the FEA Filter is mounted in a custom FEA Lid/Filter Mount (see figure 19).

The filters are located one at each of the five thermal interfaces from the dewar main shell to the CTS lid. The filters vary

Table 6. Parameters of the Suzaku/XRS blocking filters.

Serial number	Pinhole transmittance	Nominal thickness Polyimide	Aluminum	Mesh	Temperature (K)
CTS-FM-05	3.80×10^{-4}	737 Å	508 Å	None	0.060
FEA-FM-201	4.33×10^{-4}	737 Å	508 Å	None	1.3
Neon-FM-202	3.59×10^{-8}	1023 Å	1088 Å	None	17
IVCS-FM-204	2.69×10^{-8}	1025 Å	1088 Å	None	120
DMS-FM-201	1.31×10^{-5}	1060 Å	802 Å	70 lines/inch Ni (T = 78%)	250

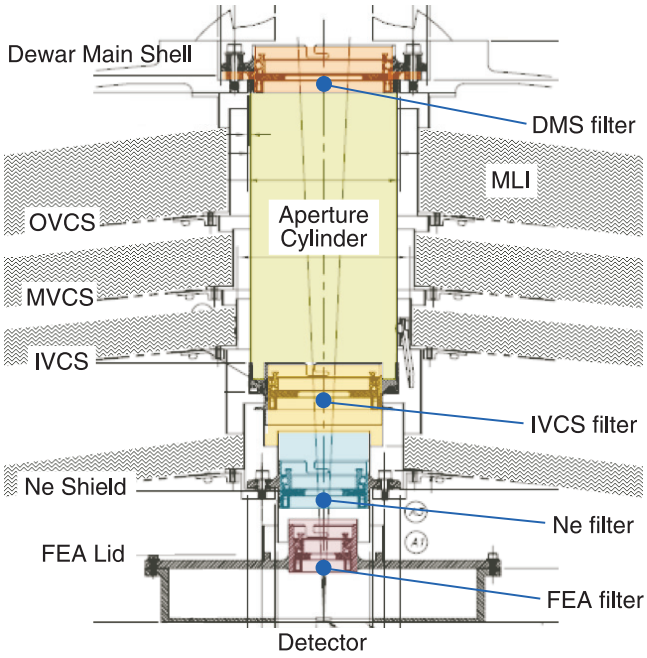

Fig. 19. Schematic view of the XRS dewar aperture.

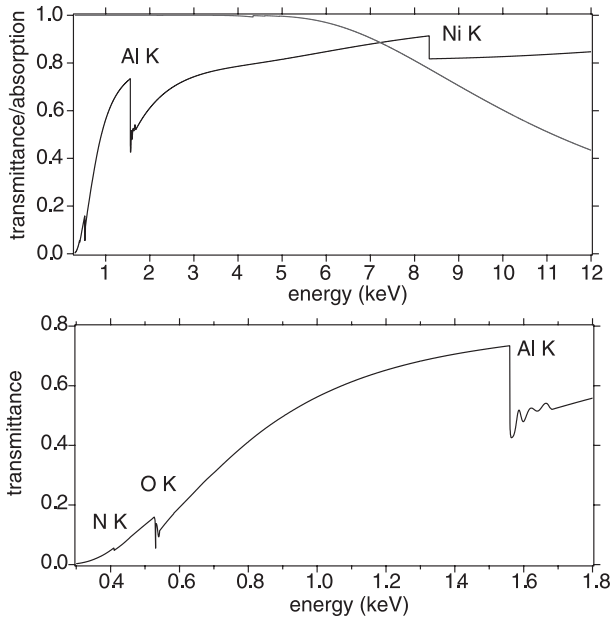

Fig. 20. The X-ray transmission of all five optical blocking filters (black) and the HgTe absorber quantum efficiency (gray). The discrete absorption edges are labeled.

in size from a diameter of 7.4 mm for the CTS filter to 30.5 mm for the DMS filter and are made of approximately 1000 Å of each polyimide and aluminum. Because of its relatively large size, additional mechanical support is given to the DMS filter with a 70 line per inch nickel mesh. The mesh covers $\sim 22\%$ of the total geometric area of the DMS filter and is about 18 μm thick (Audley et al. 1999). A summary of the physical properties of the filters, including the pinhole transmittance and the nominal thicknesses of the polyimide and aluminum layers, is given in table 6.

The photon transmittance of each filter changes dramatically over the energy band of the XRS, and, in order for the photon flux entering the XRS from the X-ray telescope (XRT) to be inferred, it must be measured as a function of energy. Because the manufacturer quotes the thickness and chemical makeup of each filter, the X-ray transmission can be determined using the photoabsorption cross sections given by Center for X-ray Optics (CXRO) at the Lawrence Berkeley National Laboratory (Henke et al. 1993). However, because the CXRO does not include the fine structure that exists near the absorption edges, and to verify the thicknesses quoted by the manufacturer, we measured the transmittance of each filter using a variable line-spaced grating spectrometer system located at Goddard (Audley et al. 1999).

Figure 20 shows the fit to the measurement of the combined transmittance of all five flight filters. The top figure shows the transmittance across the entire energy band and the bottom figure shows the energy band between 0.3 and 1.8 keV. The K-shell absorption edges of nitrogen, oxygen, aluminum, and nickel are labeled. The nitrogen, oxygen, and aluminum edges are produced by the aluminized polyimide, while the nickel edge is produced by the nickel mesh on the DMS filter, which, it turns out, is not 100% opaque across the energy band of the XRS. In the bottom figure, the extended X-ray absorption fine structure can be seen around the aluminum and oxygen edges. The curve in figure 20 is a fit to the measured data based on photoabsorption cross sections given by the CXRO in energy bands away from absorption edges, and, in energy regions near absorption edges, is based on empirical fits to the measurement to account for the fine structure. The thickness of the total filter stack, determined from the regions away from the edges, is approximately 10% larger than nominal and includes an additional oxide layer of ~ 50 Å per filter.

Table 7. Properties of filters and calibration sources.

Position	1	2	3	4	5	6
Filter	open	open	Be 300 μm	Be 300 μm	ND 10%	ND 10%
Cal. source	···	^{55}Fe, ^{41}Ca	···	^{55}Fe	···	^{55}Fe
Material	···	···	Be	Be	Mo	Mo
Hole diameter*	···	···	···	···	320(2)μm	320(2)μm
Weight*	···	···	1.006(1) g	0.988(1) g	3.565 g	3.565 g
Thickness†,*	···	···	288.7(9) μm	283.5(9) μm	200 μm	200 μm
Transmission‡,*	···	···	···	···	9.53(2) %	9.53(2)%

* Number in parentheses denotes measurement errors in.
† Thicknesses of the Be filters were calculated from their weight.
‡ Transmissions of ND filters are averages of X-ray transmission measurements.

To determine the photon flux entering the XRS dewar assembly from the detected spectrum also requires knowledge of the fractional absorption of the HgTe absorbers. The fractional absorption as a function of energy is given in the top graph of figure 20. This curve was generated using the areal density of the absorbers combined with the photoabsorption cross sections for mercury and tellurium given by the CXRO. The areal density was determined to be $69.21 \pm 0.99\,\mu\mathrm{g\,mm^{-2}}$ by measuring the mass and cross sectional area of > 40 individual absorbers all taken from the flight wafer.

7. Filter Wheel

The XRS Filter Wheel (FW), located just above the dewar aperture, external to the dewar, is designed to reduce the flux from bright celestial sources so that the deadtime of the detector is not too high. The FW provides 6 apertures that can be alternately positioned along the optical path, and 2 X-ray-emitting radioactive isotopes for in-flight calibration (figure 21). It consists of the filter wheel unit and drive electronics (FDE). The assembly of the FW was carried out by NEC TOSHIBA Space Systems, Ltd. The unit for Suzaku has several improvements over what was originally designed for Astro-E (Furusho et al. 1999). The housing of the filter wheel is 186 mm in diameter and mounted on the middle deck of the spacecraft. The total weight of the filter wheel unit is 850 ± 0.1 g. The distance between the XRS detector plane and the filter elements is 397.5 mm, where the X-ray image from the XRT has a diameter of 39.2 mm. The diameter of the filter elements is 49 mm, and the effective opening diameter is 44 mm. The filter elements are summarized in table 7. Neutral density (ND) filters of 10% transmission are made from 200 μm thickness Mo plate with 1802 pin holes of 320 μm diameter. X-ray transmission was measured by raster scans of 1.4 mm $\times$ 0.45 mm X-ray beams. Using Al Kα (1.487 keV), Ti Kα (4.509 keV), and Cu Kα (8.041 keV) lines, the transmission is consistent with $9.53 \pm 0.15\%$. The low-energy cut-off filters are Be plates of 300 μm thickness. The X-ray transmission was measured at 5 different energies (1.776, 2.294, 4.509, 8.041, and 8.400 keV) and fitted well by $272.2 \pm 0.2\,\mu$m and $267.7 \pm 0.2\,\mu$m of Be with contaminations dominated by $0.03 \pm 0.02\%$ of Fe. Gradations of thickness caused by the rolling process were found to be 6% at most and would be incorporated into the XRS response functions.

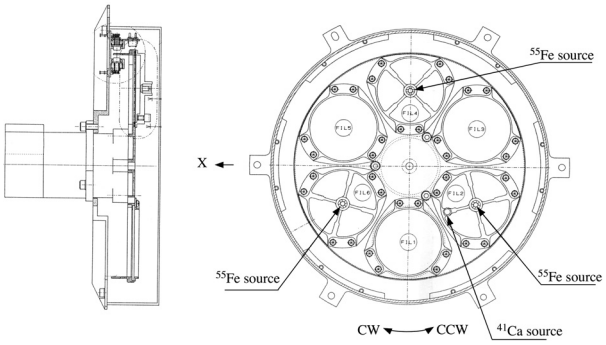

Fig. 21. Design of FW. Left: Side view in the housing, Right: Bottom view without housing.

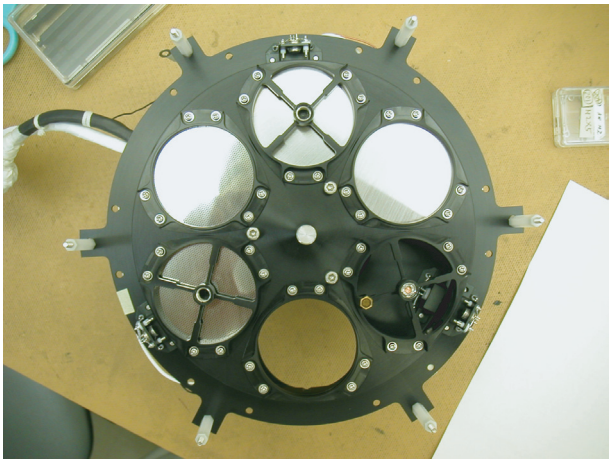

Fig. 22. Photograph of filter elements and dummy calibration sources installed on the FW disk.

Calibration sources of ^{55}Fe (Mn Kα_1: 5.899 keV, Kα_2: 5.888 keV, Kβ: 6.490 keV, $T_{1/2}$ = 2.73 yr) and ^{41}Ca (K Kα_1: 3.314 keV, Kα_2: 3.311 keV, Kβ: 3.590 keV, $T_{1/2} = 1.03 \times 10^5$ yr) are mounted at positions 2, 4, and 6 of the FW, as shown in table 7 and figure 22. The ^{55}Fe sources are electro-deposited on copper blocks and are coated by thin Ni. The ^{41}Ca source is packed in a screw-like SUS holder shielded by a 50-μm Be window. Estimated counting rates on

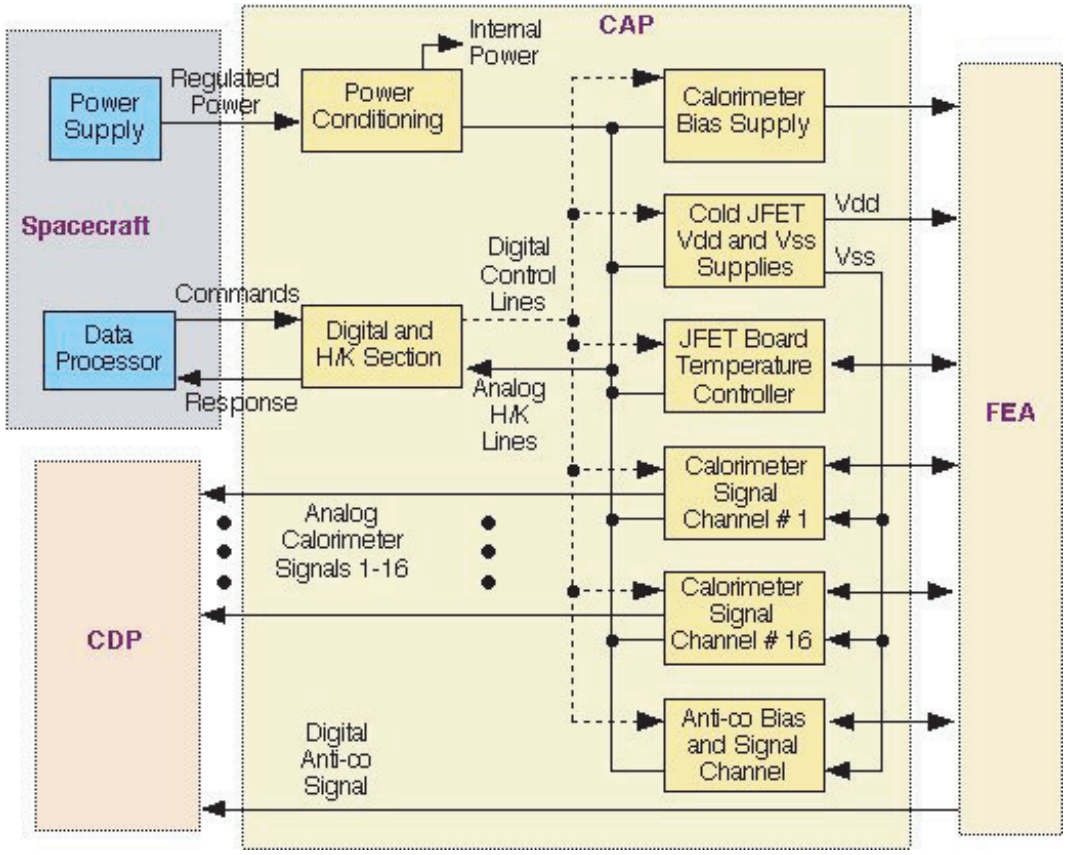

Fig. 23. Block diagram of the Calorimeter Analog Processor (CAP).

an XRS pixel at launch are $\sim 0.145\,\mathrm{c\,s^{-1}\,pixel^{-1}}$ for ^{55}Fe and $(9.2 \pm 0.6) \times 10^{-4}\,\mathrm{c\,s^{-1}\,pixel^{-1}}$ for ^{41}Ca in vacuo. In ground calibration tests, ^{55}Fe X-rays were detected through the gate valve Be window and the counting rates were consistent with prior estimates.

The FDE controls the filter wheel operation based on commands and processed position data. The main part of the electronics which controls the stepper motor consists of an HIC (Hybrid Integrated Circuit) which generates three phase control signals. By command, the FDE can rotate the filter wheel with 1 step, 20 steps (1°), and 1200 steps (60°) in a specified clockwise/counterclockwise direction. The position of the filter wheel is monitored and checked by three different methods, as the number of step signals from the HIC, the number of an optical encoder counter mounted within the motor, and the signal pattern of LED-photodiode pairs through the slits at the filter-wheel edge.

The FW was switched off at position 1 (fully open) before launch and powered on 2005 July 24, 14 days after the launch. The basic functions were tested and the ^{55}Fe source illuminated the array through the gate valve on 2005 August 3. The FW continues to be successfully exercised daily with ±60° steps to provide lifetime engineering data.

Table 8. Mass and nominal power of the electronics boxes.

	Mass* [kg]	Nominal power [W]	Max power [W]
CAP	4.95	7.8	7.8
CDP	5.89	9.95–12.0	19.8
ACHE	9.10	22.0	43.3†

* Does not include shorting plugs and EMI filters.
† When the ADR magnet is fully charged.

8. Instrument Electronics

8.1. Analog Electronics

The Calorimeter Analog Processor (CAP: see figure 23) provides power and bias to the detectors and first-stage JFET's, amplifies the detector signals, and controls the temperature of the first-stage JFET's. The CAP consists of two identical A and B sides, each of which handles 16 channels. The mass and the power of the CAP are summarized in table 8.

The cold JFET's, located within the FEA, convert the $\sim 30\,\mathrm{M\Omega}$ detector impedance to an output impedance of $2\,\mathrm{k\Omega}$ for transmission to the CAP. Their operating temperature of 130 K is controlled by the CAP.

There are 4 detector bias supplies, each of which supplies the bias voltage to 8 detectors. Likewise, there are 4 V_{dd} supplies, each supplying power to 8 of the cold JFET's.

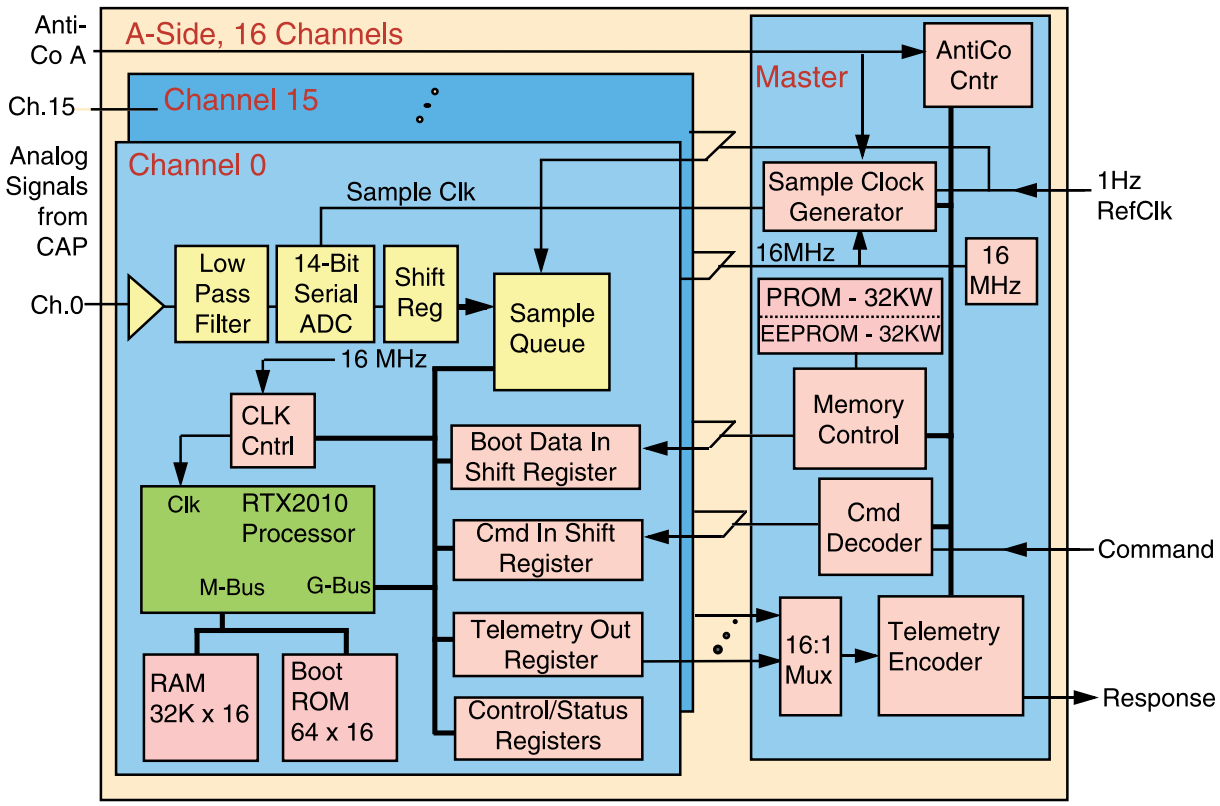

Fig. 25. CDP block diagram. There are 2 completely independent "sides", labeled A and B, for redundancy. Each side comprises a "master" circuit which handles commands and telemetry and stores the DSP code in PROM and EEPROM, and 16 DSP channels. One channel is shown in the diagram.

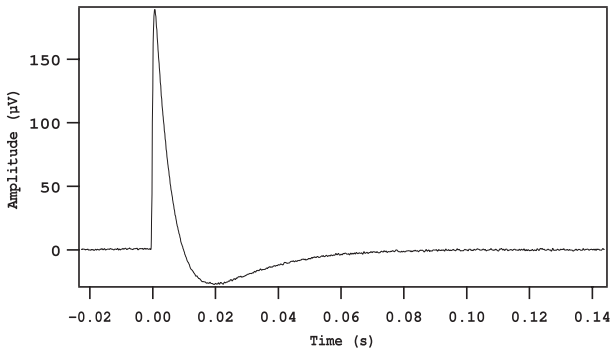

Fig. 24. A typical pulse from one detector. The X-ray pulse raises the temperature of the thermistor, thus lowering its resistance. Since the array pixels are essentially current-biased by the FEA circuitry, this causes a drop in the voltage across it. For convenience, the pulse is inverted by the CDP. The pulse overshoots its baseline because of the AC coupling in the CAP.

The CAP contains 32 amplifier circuits, one for each detector pixel. Each amplifier is implemented in a hybrid circuit package. The amplifiers have an AC gain of 20000 and a highpass knee of 10 Hz. Their output is a full differential signal (maximum 24 V), which is sent to the Calorimeter Digital Processor (CDP). The temperature stability of the amplifiers is better than 200 ppm/°C. The signals are AC coupled, with a single pole at 10 Hz.

8.2. *Digital Electronics*

The signals from the CAP are voltage pulses with a maximum amplitude of 24 V. A representative pulse is shown in figure 24. The voltage at the detector actually decreases during a pulse, but the differential output of the CAP is reversed for convenience, giving a positive-going pulse at the input to the CDP.

Due to telemetry limitations, pulses must be detected and processed on-board. This is the job of the Calorimeter Digital Processor (CDP). The CDP is configured as 32 independent channels, one per pixel, all running the same software. It also contains shared circuitry to handle communication with the spacecraft. Figure 25 shows a block diagram of the CDP.

Each channel contains an attenuator, antialias (AA) filter, 14-bit Analog-to-Digital Converter (ADC) running at 12288 Hz, a microprocessor (Digital Signal Processor, DSP) with 64 kBytes of Static RAM, and interfaces to the rest of the system.

Each channel in the CDP is responsible for a single pixel in the detector array. The CDP processing detects pulses, processes them, and sends the data to the spacecraft. Each X-ray pulse detected results in a 64-bit data packet, containing the pulse height, the rise time of the pulse, a measure of the pulse shape, a time tag with 5 μs resolution, the pixel number, and 6 one-bit flags. The flags indicate event grade, whether the anticoincidence detector fired, whether the pulse was electrically clipped at the ADC, and whether it is a "baseline" pulse.

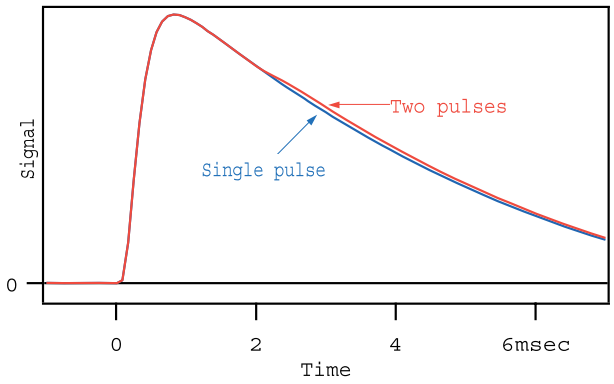

Fig. 26. A 200 eV pulse 2 ms after a 10 keV initial pulse.

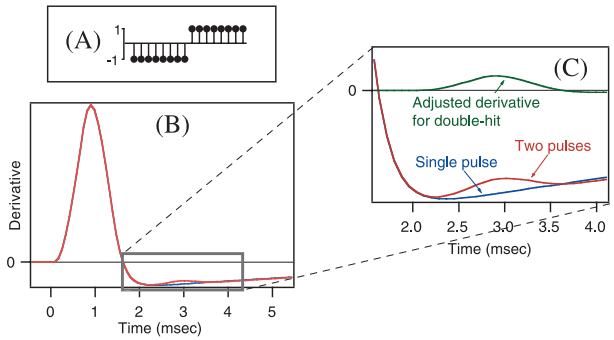

Fig. 27. (A) The form of the boxcar derivative. (B) The derivative of a single pulse, and of the double pulse from figure 26. (C) Magnified view of the derivatives where the second pulse occurs, including the *adjusted derivative*, which is the difference between the single pulse and double pulse derivatives.

Baseline pulse heights are created by processing a noise record as if it were a pulse, and are used to obtain a measure of the noise in the system.

8.3. *Pulse Detection*

The primary job of the DSP is to detect pulses in the data stream. Detecting an isolated pulse is very simple; the hard part is finding small secondary pulses on top of large ones. This is shown in figure 26, which is a simulation (without noise) of a 200 eV secondary pulse 2 milliseconds after a 10 keV initial pulse. Clearly, the secondary pulse is not detectable with a simple level discriminator, or even a simple discriminator based on the signal derivative (since the derivative never goes positive for the secondary pulse). However, the pulse detection algorithm does start with a smoothed derivative of the data. The derivative is calculated by convolving the data with a "boxcar derivative" function, as shown in part (A) of figure 27. The number of samples (the length of the boxcar) is an adjustable parameter.

The initial pulse is detected using a simple level discriminator on the derivative. The threshold is set as low as possible given the noise level in the system. In order to detect secondary pulses, the CDP maintains a copy of the single-pulse derivative shape. When an initial pulse is detected, this derivative shape is scaled by the pulse amplitude and subtracted from the calculated derivative to form an adjusted derivative. A secondary pulse is provisionally triggered when the adjusted derivative exceeds a discriminator threshold. In normal operation this threshold is set to the same level as the initial pulse threshold. The provisional trigger becomes an actual secondary pulse detection only if the adjusted derivative peaks and returns to zero within a specified length of time. Upon detection of a secondary pulse, the single-pulse derivative shape is appropriately scaled and offset, then added to the original correction curve used to calculate the adjusted derivative.

8.4. *Pulse Height Analysis*

The CDP calculates the height of each pulse by using an optimal filter (Szymkowiak et al. 1993), which is a matched filter that has been weighted in frequency space by the noise in the system. The details of this calculation are given in Boyce et al. (1999).

The filter is applied via partial convolution in the time domain. The length of the optimal filter is 2048 samples, which corresponds to 166 ms. For pulses separated by this much time, the full optimal filter is applied, giving what is known as a "hi-res" pulse. If two pulses are closer than 2048 samples, but more than 512 samples, a quarter-length optimal filter is used, yielding a "mid-res" pulse. If they are closer than that, a simple measure of the peak pulse height is used, giving a "low-res" event. Low-res events are significantly lower resolution than hi-res, having a $\Delta E/E$ approximately 5 times worse. The events in the data stream are tagged with the event grade.

In the absence of noise tones (noise at a single frequency), the mid-res pulses have approximately the same resolution as the hi-res ones. If there are noise tones, then mid-res pulses will have lower resolution than hi-res. We typically saw many noise tones during instrument testing on the ground (mostly power-line harmonics and computer vertical sweep harmonics). Once the instrument was integrated into the spacecraft at ISAS, the noise became essentially flat with frequency.

The CDP also tags events with a "secondary" flag, which indicates that an event fell on the tail of a previous event. So if a pair of pulses arrives 10 ms apart, they will both be low-res, but only the second one will be marked secondary. Secondary events suffer from reduced gain, since the detector is still warm (and hence less responsive) from the first event. It is possible to account for most of this gain error by applying an exponential correction to the secondary pulse height, based on the size of and time since the preceding pulse. All events are time-tagged, which allows us to correct fairly effectively for the reduced gain of secondary events.

It is important to note that each individual event is analyzed with the maximum energy resolution based on applying the correct pulse template; there are no resolution modes. In fact, once collecting science data, the CDP has no modes at all.

Table 9 indicates the grade for an event separated in time from a preceding event by t_1 and from a subsequent event by t_2, all three events occurring on the same pixel. This assumes that the mid-res template is 1/4 the length of the hi-res template, which is the usual case.

The fraction of events in each grade can be calculated easily, assuming a Poisson distribution of photons, using the information in table 9. The results are shown in figure 28. Figure 28

Table 9. Event grades as a function of time since previous pulse (t_1) and time until next pulse (t_2).*

	$t_1 < 35.5$ ms	35.5 ms $< t_1 <$ 142 ms	$t_1 > 142$ ms
$t_2 < 35.5$ ms	LS	LS	L
35.5 ms $< t_2 <$ 142 ms	LS	MS	M
$t_2 > 142$ ms	LS	MS	H

* H: Hi-res, M: Mid-res, L: Low-res, S: Secondary.

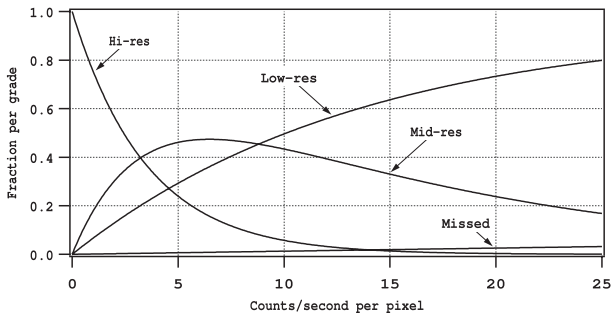

Fig. 28. The fraction of events which fall into each grade, as a function of count rate per pixel. This applies to each pixel individually.

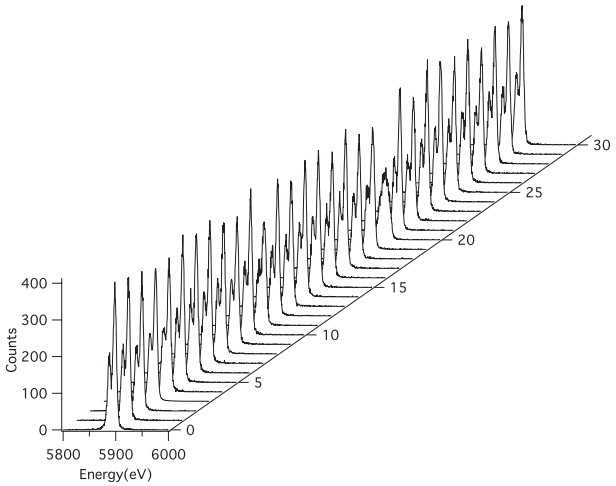

Fig. 29. Pulse-height histograms obtained using ^{55}Fe during spacecraft ground tests.

also shows an estimate of the fraction of events which are missed entirely, because they are too close to the preceding pulse. If two pulses are too close to be detected individually (about 0.7 ms apart), they will be measured as a single event, with a pulse height approximately equal to the sum of the two individual pulse heights. Such events also have a very broad range of rise times, since even a small offset in time leads to a noticeable S-shape in the rise of the combined pulse.

Along with pulse height, time, and flags, each event includes a measurement of the pulse rise time. This is useful to identify certain classes of "bad" events. We determine the rise time by fitting a straight line to a fixed number of points centered at the 50% amplitude point of the rise. Normally we use 3 samples, but this can be changed by a command. We use a fixed number of points to eliminate a source of bias in calculating the rise time. If we use all the points from, say, 10% to 90%, then there are discrete jumps in rise time between pulses with N points on the rise and pulses with $N + 1$ points. This is because the rise is S-shaped, and so adding one more point to the calculation always increases the rise time.

The CDP also processes events from the anticoincidence detector. If an anticoincidence pulse occurs anytime within an adjustable window near the beginning of a detected X-ray pulse, that event is tagged with the ANTICO flag.

8.5. ADR Control and Housekeeping Electronics

The ACHE is responsible for the control and thermal monitoring of the XRS instrument. The ACHE hardware is microprocessor based and implemented in a 4-card chassis. The ACHE has a mass of 9.1 kg and consumes approximately 22 W in its nominal mode (table 8). The ACHE hardware provides the 2-A magnet current source for the ADR recharge cycle (i.e., GCC), as well as the control circuit for driving the magnet current to maintain tight temperature control at the nominal operating temperature of 60 mK. The ACHE also has 32 sensor channels which perform 4-wire temperature measurements using a lock-in amplifier approach. The first 16 channels monitor the colder parts of the instrument (high resistance) using an excitation current of 9.6 nA. The second 16 channels monitor the warmer parts of the instrument and use an excitation current of 1 μA. The ACHE also provides voltage sources for the IVCS and DMS filter heaters, and current sources for the heat switch and mass gauge heaters.

9. Pre-Launch Tests and Calibration

The XRS underwent extensive testing at the He Insert subsystem-level at Goddard during the winter of 2004 (Cottam et al. 2004). Testing at the full instrument level took place at SHI in the summer of 2004, prior to the final integration onto the spacecraft at ISAS/JAXA in 2004 September (Cottam et al. 2006). Then, a series of spacecraft functional and environmental tests were performed until 2005 April at ISAS/JAXA (Ota et al. 2006). In figure 29 we show the individual pixel responses to an ^{55}Fe source obtained during ground calibration in 2004 September. The resolution is typically 6 eV across the array (FWHM). Only one channel has a very energy-dependant excess broadening (about 14 eV at 6 keV). We characterized the spectral performance of the XRS from the energy scale, the line spread function, the instrument background, and the efficiency of various components of the effective area. In

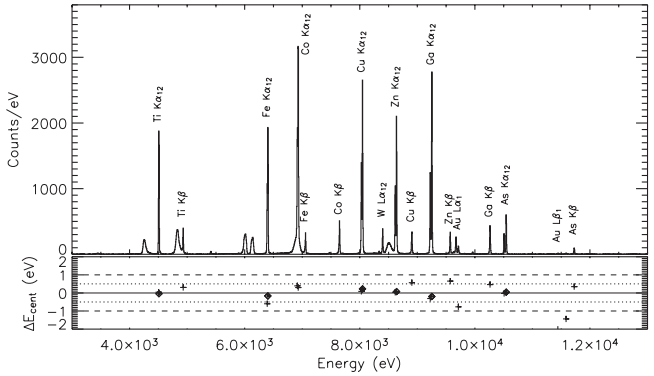

Fig. 30. An energy-corrected spectrum obtained during ground calibration and the residuals between the measured and laboratory energies for the brightest lines. The diamonds represent the Kα lines that were used to generate the energy scale.

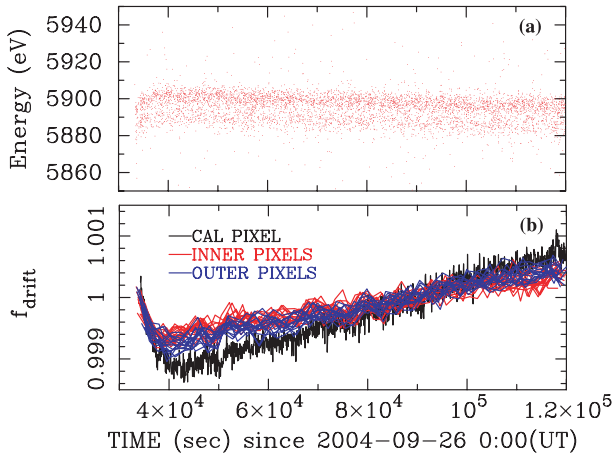

Fig. 31. Example of XRS pixel gain drift (a) and drift correction factor, $f_{\rm drift}$ for the calibration pixel, inner 15 pixels, and outer 15 pixels of the array (b). In panel (b) $f_{\rm drift}$ was derived every 100 events from the FW source (method 2). A GCC was carried out at 23:17 on 2004 September 25 (UT).

the following sections we will present the main results of our instrument characterization and ground calibration.

9.1. Energy Scale

The XRS energy scale, which maps the measured pulse heights to the energy of the incident photons, is a complex, non-linear function that depends not only on the design parameters of the XRS array and the pulse detection algorithm, but, as discussed in subsection 3.2, also on the operating conditions, including the thermal environment seen by the array and the photon flux impinging on the array and frame. Because of the inherent complexity, the energy scale is determined by empirically fitting measured pulse heights from known energy sources to a polynomial function.

During ground calibration, the energy scale is determined by illuminating the array with fluorescent emission lines. We were able to generate energy scales that are accurate to better than $\Delta E_{\rm centroid} \sim 1.0\,$eV (figure 30). Because the energy scale depends on the specific operating conditions, a new energy

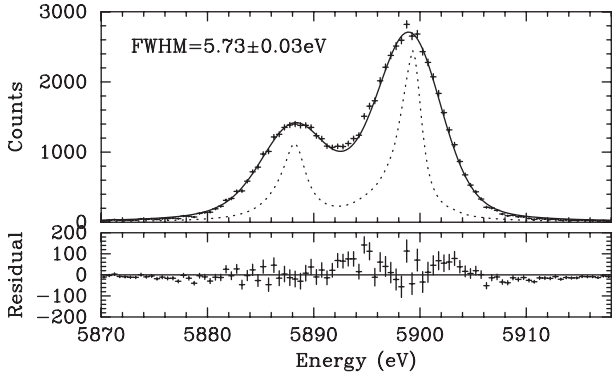

Fig. 32. Composite spectrum of Mn Kα_1 and Kα_2 for all XRS pixels except for the calibration pixel, and pixels 11 and 20, fitted to the intrinsic line shape (dashed curve) of Mn lines produced by an ^{55}Fe source. The solid curve is the best-fit to this profile assuming a Gaussian energy resolution kernel. The data were taken on 2004 September 28 at ISAS/JAXA, with the mechanical cooler running.

scale must be generated in-flight using both onboard radioactive sources and astrophysical sources.

Temporal changes in gain affect both the energy scale and composite energy resolution of the array. In figure 31a, an example of the gain drift curve is shown. An apparent energy shift of the Mn Kα line by 10 eV was observed during a 24-hour running test.

The simplest way to correct the gain drift is to monitor the Mn Kα line energy with the calibration pixel and apply its gain correction factor to the thirty active pixels (method 1). The gain correction factor, $f_{\rm drift}$, was derived by calculating a ratio between the observed mean energy channel and the mean Mn Kα energy of 5894.397 eV (a weighted mean energy of the eight Lorentzian line components) every 100 events. This method is effective when the gain variation is due to changes in the $\sim$ 60-mK heat sink temperature. However, as mentioned previously, different behavior among the pixels was observed; the inner 15 pixels show the smallest changes and the outer 15 pixels show more, and the calibration pixel shows the largest shift in energy (figure 31b). Corrections using method 1 resulted in resolutions of $\sim$ 6–8 eV. As shown in subsection 3.2, we think that the temperature variations of the Ne and He baths cause small changes in a stray power seen by the array and affect the pixels differently depending on their positions.

^{55}Fe and ^{41}Ca sources are attached to the filter wheel and can be placed in the field of view of the array (see section 7), so we next performed the correction for each pixel by monitoring the Mn Kα line from the filter-wheel source (method 2, figure 31b). This self-calibration significantly improved the resolutions: the fitting of the composite XRS spectrum yields a FWHM of $5.73 \pm 0.03\,$eV (figure 32) and most of the pixels have a FWHM of 5–6 eV.

The differences in behavior with temperature variation make the drift correction algorithm complex. Although self-calibration (method 2) is very effective, use of the FW source would increase the unrejected background intensity from electron and photon escape events, which would compromise observations of faint objects. The gross cycle control (GCC) of the ADR is considered to be the dominant influence

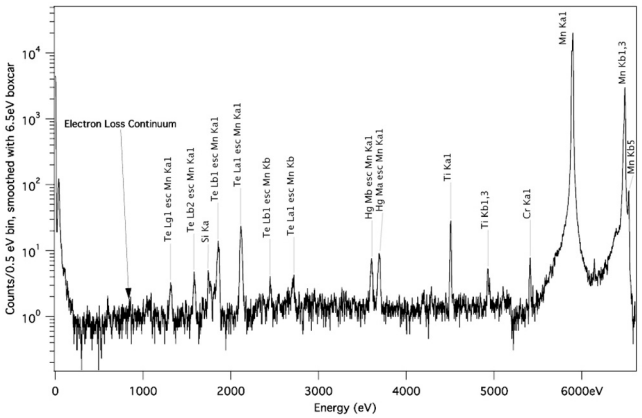

Fig. 33. The broadband XRS response to an ^{55}Fe source. The low energy redistribution tail includes fluorescent escape lines from the Hg and Te in the pixel absorbers.

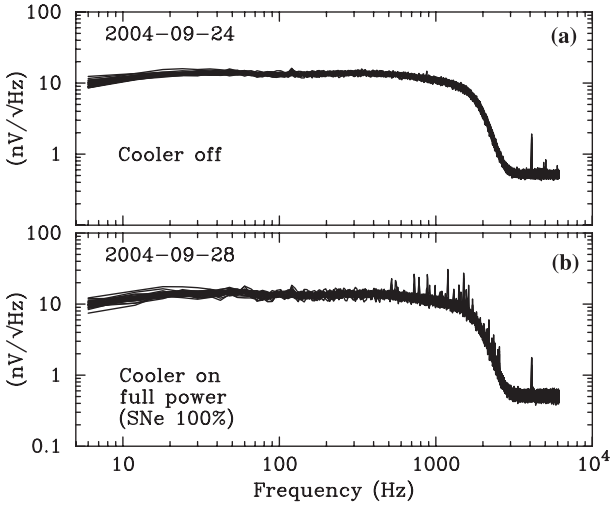

Fig. 34. Noise spectra of XRS pixels with the mechanical cooler off (a) and on at nominal full power and 52 Hz during the 2004 September functional test (b).

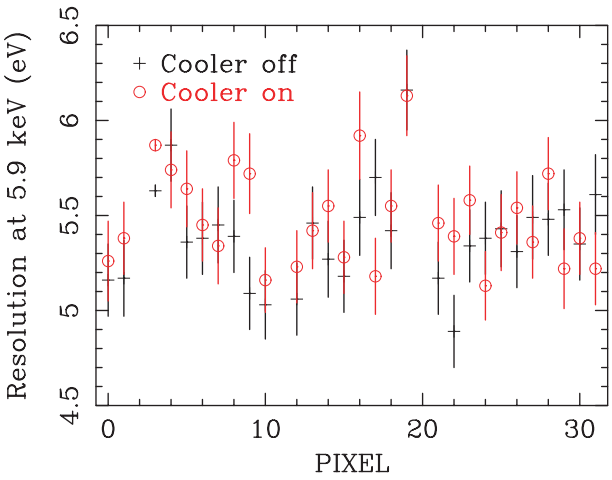

Fig. 35. Comparison of pixel resolution between the cooler-off and cooler-on data. The pixels 11 and 20 are outside the graph.

on the He and Ne temperature variations. We found through the ground tests that the gain is more unstable for the first 2–3 hours after a GCC (see figure 31). Thus, periodic GCC operation would allow the gain-drift repeatability to be measured and, eventually, used to improve the gain drift correction. The house-keeping data will be also useful for correcting the differential gain drift between the calibration pixel and the main array. The ground experiments were thought to be out of equilibrium and the gain was likely to be more stable in orbit.

9.2. *Line Spread Function*

The XRS Line Spread Function (LSF) consists of a Gaussian resolution kernel and a low energy tail. The resolution kernel is primarily determined by phonon and Johnson noise. These produce a Gaussian distribution in the measured energy around the nominal value. In addition to the Gaussian core, the XRS LSF contains a low-energy shoulder that is caused by photon and electron escape events.

The LSF has been measured by illuminating the array with a ^{55}Fe electron capture source and several characteristic fluorescent emission lines. Figure 33 shows the measured XRS response to the Mn Kα line from the ^{55}Fe source. Except at low energies where the electron loss continuum begins to contribute, the XRS resolution kernel can be successfully described by a single Gaussian. The composite resolution for the array, excluding two outlying pixels, is $\Delta E(\mathrm{FWHM}) < 6\,\mathrm{eV}$ at 6 keV. The energy resolution is only weakly energy dependent, increasing from $\sim 6\,\mathrm{eV}$ at 5.9 keV to $\sim 7.5\,\mathrm{eV}$ at 9.3 keV.

Microphonic noise from the mechanical cooler (see subsection 5.3) was one of our concerns, and its impact was measured in two configurations, during the instrument-level performance verification test at SHI in 2004 July–August with 10% solid neon, and during the spacecraft test phase with 100% solid neon.

In the fully integrated configuration on the spacecraft, noise spectra of the detector channels were very clean when the mechanical cooler was off. The noise level was 13–14 $\mathrm{nV\,Hz^{-1/2}}$ up to 1 kHz, and there were no line components (figure 34a). When the mechanical cooler was operated with full power, there were several line components of 10th or higher harmonics in the noise spectra (figure 34b). Since the frequency range was high ($\gtrsim 500\,\mathrm{Hz}$), however, it did not affect the energy resolution at all, and the instrumental width of $5.73 \pm 0.03\,\mathrm{eV}$ (figure 32) was unchanged from that obtained while the cooler was off, within statistical errors. A comparison of the instrumental width for each pixel is also shown in figure 35.

On the other hand, during the subsystem-level test with 10% neon, there were fundamental and harmonic line components in the low frequency range of the noise spectra, and the energy resolution became 6–8 eV (FWHM). However, the test configuration was quite different from that on the spacecraft, i.e., (1) the dewar was set on a dolly and not firmly attached to the spacecraft, and (2) long GSE harnesses were used instead of the flight harnesses. Therefore, we could not pinpoint the cause of the degradation.

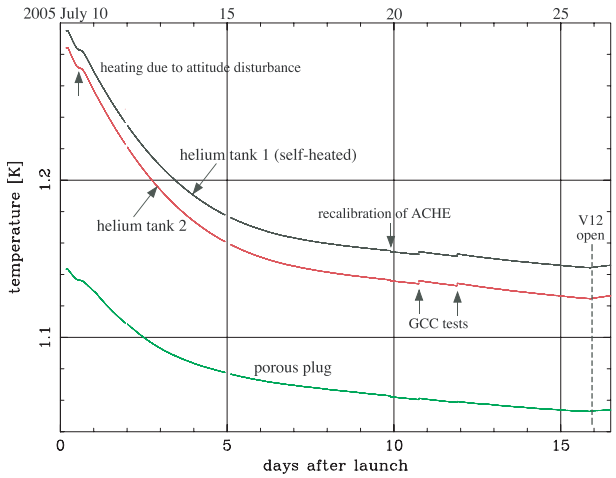

Fig. 36. Temperature history of the He tank (sensors 1 and 2), and the porous plug, from launch to day 16.

In conclusion, the mechanical cooler does not degrade the detector performance, at least in the initial phase when the amount of neon is $\sim$ 100%. In fact, this was verified using the inflight data. At the end of the mission, its impact, at worst, would not have been large, and the energy resolution of 6–8 eV (FWHM) could have been achieved even in the worst case.

9.3. Effective Area

The effective area of the XRS includes the effective area of the telescopes, the overlap fraction between the mirror point spread function and the detector pixel absorbers, the transmission of the five optical blocking filters, the detector quantum efficiency, and electronic deadtimes. The full XRS effective area, based on everything measured prior to launch is shown in figure 2 in section 1. The discrete structure in the effective area curve is dominated by the quantum efficiency of the HgTe absorbers at high energies and the transmission of the blocking filters at the low energies, both of which have been characterized extensively on the ground.

10. In-Flight Performance of the XRS

10.1. Dewar System

The final low-temperature top-off of the He cryostat was carried out 2 days prior to launch. The cryostat was filled to 30.5 liters (corresponding to 92% of the available volume) at 1.6 K. The helium was then pumped to about 1.3 K before closing the fill and vent lines for launch. During the He servicing the solid Ne was cooled to about 13 K and then began to slowly rise.

Before the detector could eventually be cooled to its operational temperature of 60 mK, a number of critical steps were required to establish the proper thermal conditions. The dewar He vent valve was successfully opened 235 s after launch in order to begin pumping the He bath while there was still a positive force due to acceleration on the He. This was required in order to establish the proper temperature gradient across the porous plug. The Ne vent valve and the He fill valve (down to the internal cryostat valve, which was closed prior to launch) were opened at about 27 minutes into the flight. The ACHE electronics were powered up 24 minutes after launch and temperature data were transmitted to the ground station at Uchinoura after the first Earth orbit. The data confirmed that all of the temperature sensors were reading nominally, indicating that the dewar system had survived launch and that the porous plug had the proper temperature profile. With the He vent line open, the He temperature began to drop as expected. In figure 36 we show the temperature profile for the first $\sim$ 16 days of the mission. It can be seen that the He bath temperature had reached about 1.12 K, and was ultimately heading down to about 1.1 K, before the main shell evacuation valve, V12, was opened on day 16. Comparing the temperature of the liquid helium (thermometer no. 2) and the porous plug, one can use the data plotted in figure 13 to infer that the He mass flow rate was about $32\,\mu g\,s^{-1}$. This implies a net heat load at that time of $\sim 690\,\mu$W into the the liquid helium (but without the contribution from the ADR.)

On day 16 of the mission, the first ADR cycle was successfully conducted. The ADR cycle was initiated during a real time pass to verify that it had started properly, and then the cycle was allowed to continue during the next orbit. Upon acquisition during the subsequent pass, it was found that the ADR system was locked in tight temperature control at 60 mK.

A total of seven ADR cycles were run before the liquid helium was exhausted. Due to various tests and problems with early spacecraft operations, and eventually with the liquid He cryogen, none of these ran to completion, but two ran normally for more than 23 hours, and the extensive data taken during ground tests could be used to reliably extrapolate these results to full cycles. The hold time was about 25% longer than on the ground, largely due to lower cryogen temperatures resulting from radiative cooling of the dewar main shell to $\sim$ 250 K. The hold time is inferred to be about 38 hours with a recharging time of about 49 minutes. Analysis of the heat loads generated by recharging the ADR during prelaunch tests allowed us to determine the component heat loads (FAA salt pill ordering, heat switch getter heater power, and magnet hystersis and eddy current heating). The results are that the time-averaged heat generated by the ADR recharge is 150 μW for a 38 hour hold time, and 184 μW if a 24 hour hold time is imposed for operational convenience. Taking into account the vapor cooling return from the heat input, we obtain that the total, time-averaged heat into the He cryostat is $\sim 812\,\mu$W, assuming a 24 hour operational hold time. Given our estimate of 30.1 liters remaining prior to opening V12, this would give a projected lifetime of 3.7 years, which would have been limited to about 3.34 years by the Ne dewar.

All aspects of the ADR on-orbit performance exceeded design goals, as shown in table 10.

As shown in figure 37, following the initial increase from its liquid He cooled, temperature at launch, the neon temperatures decreased to $\sim$ 15 K, which is lower than the requirement of 17 K. On July 11, the mechanical cooler was turned on, just one day after launch. The operating power was increased in several steps, reaching the full power of 34.7 W on July 21. After the cooler was successfully put into operation, the VCS temperatures started decreasing, and reached 96 K on July 25 (see figure 38). The temperature of the main shell surface was

Table 10. On-orbit ADR performance.

Regulating temperature	60.0 mK
Temperature fluctuations	1.7 μK rms
Long-term stability	$< 1\,\mu$K
Hold time at 60 mK	38 hr
Recycle time	49 min
Operational duty cycle	97.9%
Heat load to LHe/recycle	21.0 J
FAA ordering*	12.3 J
Gas gap heat switch heater	2.9 J
Magnet hysteresis and eddy current heating†	5.8 J
Average heat load from ADR (38 hr cycle)	150 μW
Average heat load from ADR (24 hr cycle)‡	184 μW
LHe lifetime with 24 hr cycle	3.7 yr

* The ordering energy scales with the length of the previous cycle.
† According to tests done on the Astro-E magnet, this is dominated by hysteresis losses. It amounts to about 0.3% of the stored magnetic field energy.
‡ We assume most recycles would be done early for convenience in scheduling. Effective duty cycle would still exceed 98% if slews and SAA passages are scheduled into recycle time.

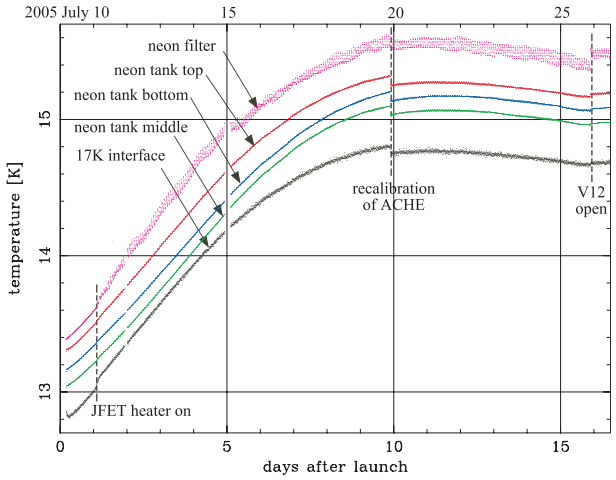

Fig. 37. Temperature history of the Ne tank (top, middle, bottom), the 17 K interface, and the Ne filter, from launch to day 16.

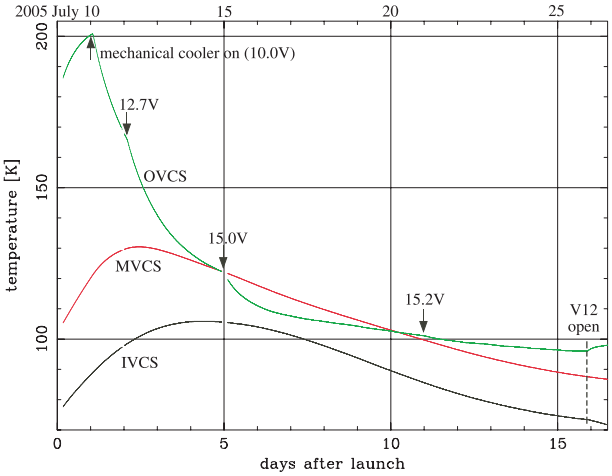

Fig. 38. Temperature history of IVCS, MVCS, and OVCS, from launch to day 16.

248 K at that time, very close to the anticipated value of 250 K, verifying that the dewar surface and radiator panel worked as designed.

Figure 39 shows the calculated heat flow based on the inflight temperature history before V12 opened on July 25. The total heat input to the Ne tank was 172 mW, and the expected lifetime of solid neon was 3.34 years. Therefore, we demonstrated that the dewar survived the launch environment and achieved the thermal performance in orbit which could achieve its design goal of greater than three years.

Once the main shell evacuation valve was opened on July 25, it was immediately apparent that internal dewar temperatures began to change in an unexpected manner. The OVCS and MVCS began to warm while the IVCS cooled more rapidly. The Ne shield showed a sudden drop in temperature while sensors on the He cryostat exhibited a reverse trend and started warming. It was quickly realized that these profiles were all consistent with gas entering the dewar guard vacuum and thermally shorting out the isolated components within the dewar. All three of the dewar vent valves (i.e., He, Ne, and main shell evacuation) are located interior to the spacecraft, and it is now considered all but certain that the spacecraft venting area was too small, creating a large flow impedance out to space. With the He and Ne vent gases as a source, along with the inevitable outgassing of spacecraft materials, the interior spacecraft pressure, and thus dewar guard vacuum pressure, are not sufficiently low enough to prevent gas conduction and adsorption within the dewar. For the dewar, He and Ne gas entering the vacuum space are the main issue. Given the nominal boil-off rate of the He and sublimation rate of Ne, one can calculate the likely partial pressures of He and Ne for an assumed spacecraft vent area. We estimate that the pressures are $\sim 10^{-6}$ and 10^{-5} torr, respectively, assuming a probable spacecraft vent area of 0.1 m^2. The He pressure alone would have to have been at least three orders of magnitude lower in order not to be a significant heat load term on the He cryostat. The compromised dewar guard vacuum resulted in the complete loss of liquid He on 2005 August 8, about 29 days after launch. The instrument electronics and mechanical cooler remain powered on for on-orbit engineering data. All of the systems we can monitor continue to perform nominally, given the current thermal conditions within the dewar.

But before the He was completely exhausted, it was possible to successfully operate the microcalorimeter array and demonstrate its performance in space, along with the associated readout electronics.

10.2. Detector System

10.2.1. Energy resolution and gain stability

The XRS calorimeter operated in orbit long enough to obtain spectral data from the calibration pixel and briefly from the whole array using the filter-wheel source. The anticoincidence detector became operational as soon as the electronics were powered and is still functioning. Background data from the

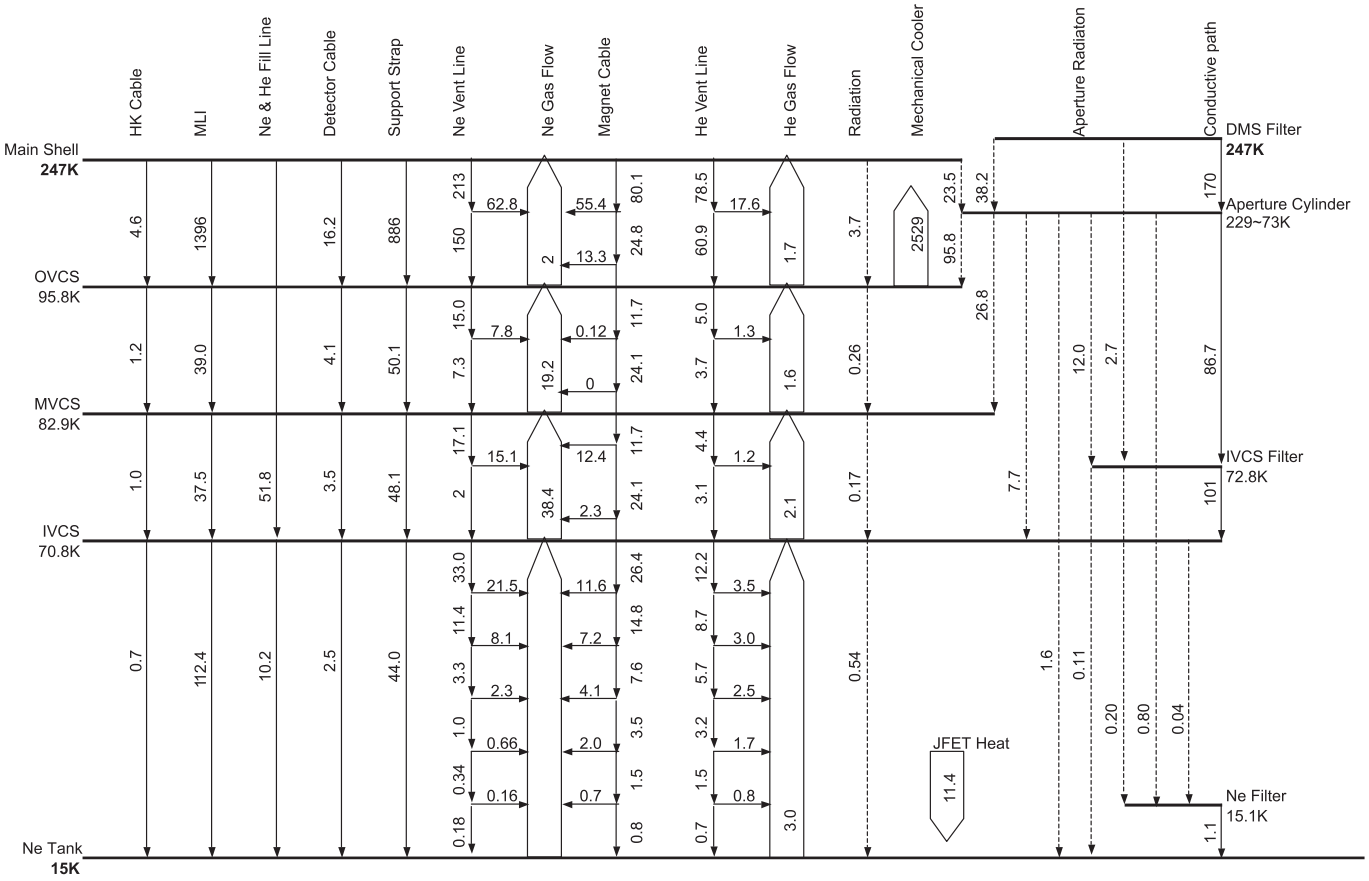

Fig. 39. Heat flow inside the Ne dewar, based on in-orbit temperature history prior to opening V12. The mechanical cooler is operated at 35 W. All the numbers are in units of mW. The total heat input to the Ne tank is 172 mW, and the expected solid neon lifetime is 3.34 years.

array were also analyzed.

In figure 40 we show a portion of the temperature profile of the thermometers on the salt pill and CTS as well as the magnet current versus time following the first GCC. One can see excellent stability between the SAA passes, which are indicated by the shaded regions about 100 minutes apart. During the SAA passes, the salt pill temperatures and ADR current drop and recover in a manner indicative of additional heat being deposited in the CTS. The ACHE controls the CTS temperature by lowering the salt temperature to compensate for the added temperature drop along the thermal path from the CTS to the salt, as evidenced by the drop in magnet current and the temperature of the thermal bus bars, which are at an intermediate point in this path. The thermometers also show extra noise during the SAA passages that is probably due to localized heating of the thermometers by direct particle hits, but this heat input is outside the bandwidth of the ADR control loop. With the system in closed-loop control, it is difficult to estimate the integrated heat load during SAA. Comparing the magnet current on the pre- and post-sides of the SAA gives only an upper limit the heating, and the temperature drop along the thermal bus indicates only the energy deposited in the CTS. Power input from SAA protons should be roughly proportional to mass, and the CTS is only about 75 g of the 1830 g total mass of the cold stage.

A more sensitive method for estimating this heat input was afforded by data when the salt pill was cold but the magnet current was zero and there was no active temperature control. This occurred about a day after the data in figure 40 were obtained, when the spacecraft was in safe hold. At this time, the ACHE had ramped the current to zero, the detector system cooled rapidly and then started drifting up slowly due to the parasitic heat input. Temperatures were indicated by the thermometry and also by the microcalorimeter pulse height gain. In this case the CTS thermometers heat up by about 1.2 mK during the strongest SAA pass while the salt pill bus thermometers heat up by about half this amount. The thermometers then cool after the SAA, but the salt pill and CTS are both about 0.05 mK warmer than prior to the pass. This indicates that heat is being absorbed in the CTS and the salt pill, with the larger temperature drops during the SAA passages due to the part of the extra heat input directly to the CTS and the limited thermal conductance between the CTS and ADR thermal bus. Moreover, the pulse heights are slightly lower after the SAA pass by an amount consistent with this temperature change.

To see if this is physically reasonable, we estimated the heat deposited from the SAA by integrating the SAA spectrum above 100 MeV and assuming this energy, mostly protons with energies around 100 MeV, is absorbed in the salt pill and

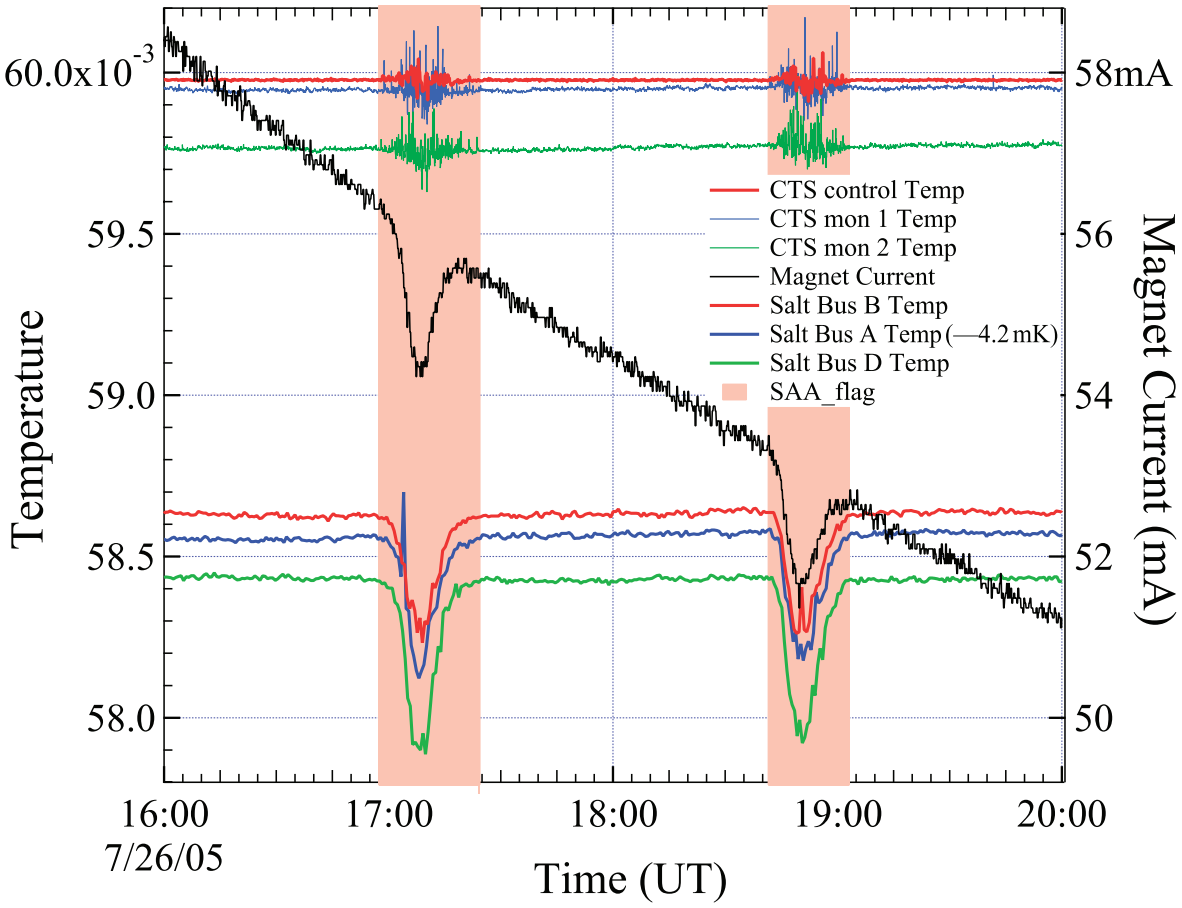

Fig. 40. Plot of the CTS and ADR salt pill thermometers and magnet current during a four hour interval following the first ADR cycle to 60 mK. The system properly regulates in tight temperature control by steadily ramping down the current. The two shaded regions correspond to passage through the two peak SAA passes for this day. The heating effects can be seen on the control system during these times, but the system recovers afterwards, indicating negligible heating.

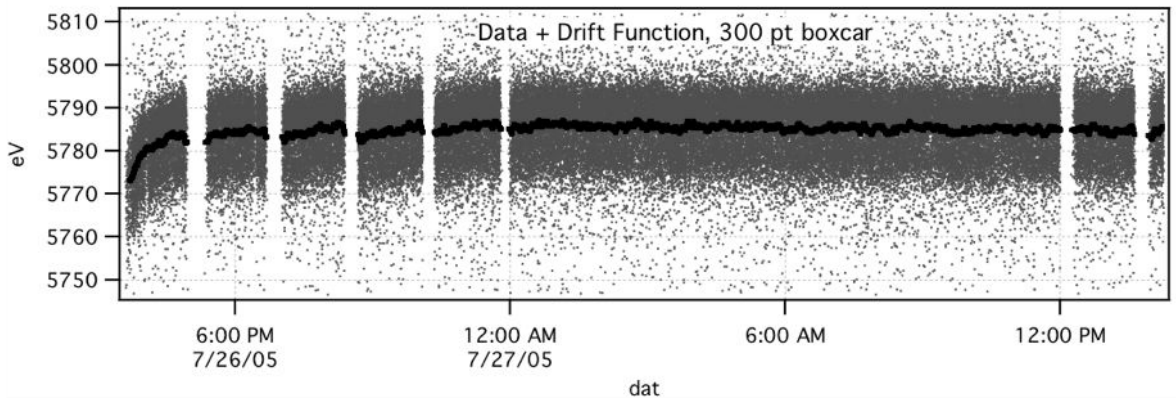

Fig. 41. Pulse height vs. time, showing the magnitude of the gain stability.

CTS. A value of 0.6 mJ was obtained. If one now adopts the measured value of the heat capacity of the salt pill ($\sim 9.9\,\mathrm{J\,K^{-1}}$ below about 80 mK), one obtains an expected temperature step of 0.06 mK, consistent with what was observed. So, although observable on such a cold system, the effects of charged particle heating are small and would not have significantly affected the thermal performance of the ADR and detector systems.

The calorimeter pulse height gain was very stable, needing only minor correction for drift even after cycling the ADR and after passage through the SAA. Figure 41 is a gain history plot from the first 24-hour period after the first GCC cycle.

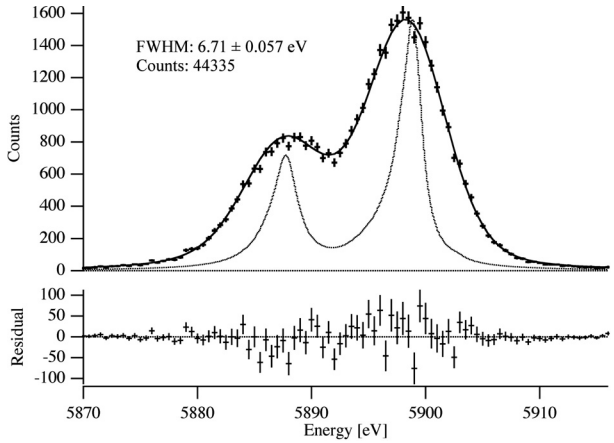

Fig. 42. In-flight, gain-corrected pulse height spectrum obtained from the data shown in figure 41.

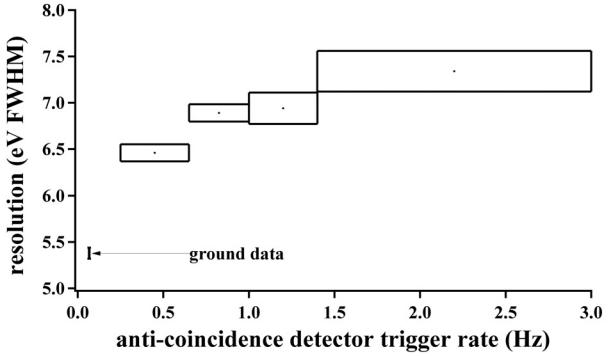

Fig. 43. Energy resolution vs. anticoincidence rate. The horizontal extent of the boxes represents the range of anticoincidence rates used to define the time intervals for data acceptance, and the vertical extent is the $\pm 1\sigma$ for the resulting line fit using hi-res events. The leftmost box is from ground data.

The data gaps correspond to the SAA crossings. The XRS was operated through SAA passage, but the large dead time from the high particle flux in the SAA resulted in an absence of detected X-rays from the calibration pixel. The resulting gain-corrected resolution from that first 24-hour interval was 6.97 ± 0.04 eV on the calibration pixel, using both "hi-res" and "mid-res" grade primary events. Using hi-res only, it was 6.71 ± 0.06 eV (figure 42).

In order to evaluate the performance of the rest of the array, the filter wheel was rotated into a position that allowed X-rays from an ^{55}Fe source to pass through the Be window of the XRS gate valve. Due to the combination of multiple satellite safe holds in the early operation of Suzaku and the effects of the helium in the XRS guard vacuum, there was only a 13-hour interval of good data while the filter-wheel source was in place. The composite resolution of the entire array during that interval was 7.82 ± 0.07 eV, with the resolution of all pixels (except the two known outliers) falling between 6.94 and 8.70 eV. The resolution of the calibration pixel was 7.19 ± 0.07 eV during the same time interval. Anomalous triggered events during this time interval indicated that even this integration was contaminated by He adsorption onto the calorimeter.

The slight degradation of the resolution in orbit from 6 eV to 7 eV appears to be another manifestation of the frame-heating effect. The resolution of the calibration pixel was correlated with the particle rate measured by the anitcoincidence detector, as illustrated in figure 43. The noise levels of all the pixels were also correlated with the particle rate. Before launch, the interaction of cosmic rays with the frame was seen as more of a problem for dead time than of noise, since most cosmic rays produce events in the pixels that exceed the $\sim$ 50-eV trigger threshold. After launch, we used two methods to estimate the spectrum of energy into the frame below the frame-event threshold. In the first, we used a coarse anticoincidence-detector spectrum that had been determined by stepping its threshold, and we scaled this to that expected in the calorimeter frame assuming domination by minimum ionizing particles. In the second we used a GEANT simulation. Assuming that the $\sqrt{N(E)E^2}$ noise term determined for X-rays into the frame holds for 100–150 keV energy depositions, both estimates of the spectrum of energy deposited into the frame reproduce the scale of the resolution degradation observed, though the rate dependence is not precisely reproduced. Nonetheless, this result supports the hypothesis of noise originating from frame heating by cosmic rays. Lowering the calorimeter pulse threshold would have ameliorated this effect to some extent by allowing more of the cosmic ray interactions in the frame to be identified as events in the pixels rather than contributing to the noise. For future microcalorimeter spectrometers, a better solution is to minimize the frame area and to improve heat sinking.

10.2.2. Background and operation of the anticoincidence detector

The anticoincidence detector was operational for two weeks prior to the first ADR cycle, providing a preview of the particle background and allowing experimentation with the anticoincidence threshold. Outside of the SAA, the measured rate ranged from 0.3 to 2 c s^{-1} in the detector (1 cm^2 area), and the rate was inversely correlated with the geomagnetic cut-off rigidity, as expected. The threshold experiments showed that roughly half of the events deposit more than 430 keV (the highest setting for the threshold). Thus the spectrum is much harder than expected for minimum ionizing particles alone, for which 80% of the events would have been below 430 keV. A preliminary attempt to simulate secondary particles using a GEANT model made the spectrum somewhat harder, but still did not match the data.

We evaluated the XRS instrument background with the gate valve closed in a continuous 37103 s interval between crossings of the SAA. The science array experienced 850366 valid triggers between 0.1 and 12 keV in the 30 pixels. To identify pulses from frame events, we used a simple algorithm developed from analysis of the ground background data; this algorithm uses a single correlation interval of 0.5 ms and rejects groups of correlated events of as few as two events. The calibration pixel is included in the screening for correlated events because electrons that escape upon X-ray absorption in the calibration pixel can be detected on the main array (Kilbourne et al. 2006). More sophisticated screening that would, among other tests, consider the energy of the calibration pixel events and use a shorter coincidence

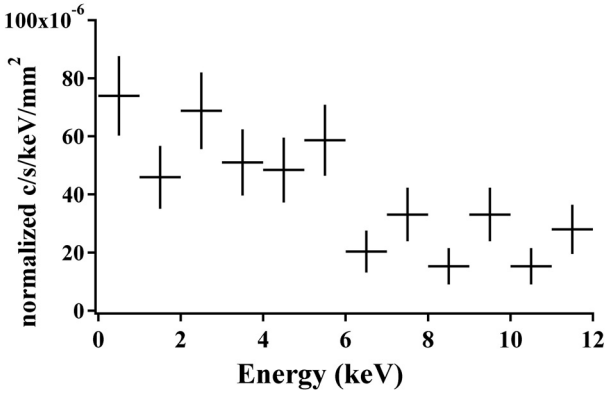

Fig. 44. XRS residual background spectrum.

window for pairs would minimize dead time without sacrificing the effectiveness of the screening, but this software was not developed. After removing events within 0.5 ms of another event and events with the anticoincidence flag, we had 207 events remaining. This corresponds to a rate of $5 \times 10^{-2}\,\mathrm{c\,s^{-1}\,cm^{-2}}$ (0.1–12 keV). The spectrum of the background events (excluding low-resolution events, which removes 14 events) is shown in figure 44; there are no lines apparent with these statistics. The average rate in the anticoincidence detector during that time interval was $0.9\,\mathrm{c\,s^{-1}\,cm^{-2}}$. If this rate were generated by minimum ionizing particles, then the background rate in the calorimeter after applying the anticoincidence veto would be $9 \times 10^{-4}\,\mathrm{c\,s^{-1}\,cm^{-2}}$, so the measured residual background is dominated by secondary particles, as expected. The rate of frame events (for which one group of correlated calorimeter pulses is considered a single event) also works out to $0.9\,\mathrm{c\,s^{-1}\,cm^{-2}}$ of frame area, though the different effective thresholds and the shielding of the anticoincidence detector by the calorimeter chip make it unlikely that the two rates refer precisely to the same population of events.

Another view of the particle environment is provided by counting all events that involve direct deposition of energy in a calorimeter absorber and the anticoincidence detector. Because there is a narrow acceptance angle for incident particles to hit an absorber and the anticoincidence detector but not the calorimeter frame, we must identify the frame events that also contain a pulse from a direct absorber hit. This is easily done by taking the ratio of the biggest pulse to the second-biggest pulse in a frame event cluster. The pulses of most frame events are similar in energy, but there is a distinct population for which the biggest pulse is greater than six times the height of the next biggest pulse. Tallying the veto-flagged events among these pulses and the isolated pulses (making no energy cuts) results in a rate of $0.55\,\mathrm{c\,s^{-1}\,cm^{-2}}$. Even this rate is likely to be dominated by high-energy secondary particles because the range in cut-off rigidity sampled by the Suzaku orbit should have reduced the $1\,\mathrm{c\,s^{-1}\,cm^{-2}}$ primary cosmic ray rate (in low Earth orbit in a flat detector at solar minimum) by more than a factor of five. More sophisticated GEANT models are needed to understand the nature of the secondary particles and what future designs could be implemented to reduce the residual instrument background.

10.3. Detector Housing and Electronics

The in-flight performance of the FEA has been nominal through one year on-orbit. The three major performance criteria are 1) structural integrity, 2) thermal contact to the refrigerator, and 3) noise performance of the JFET first stage preamplifiers. We were able to confirm that all three items were unchanged from ground characterization during the period of normal operation before the evaporation of the liquid helium. The structural integrity of the CTS suspension, the JFET suspension, the CTS thermal bus, and the wiring layers are easily verified by the fact that all of the tensioned leads are intact and show no unusual microphonic response on-orbit. The thermal contact to the refrigerator is also unchanged from ground operations showing a nominal 1.7 mK temperature difference between the CTS and the salt pill bus thermometers. We've also been able to monitor the noise performance over the year since launch, which is the topic for the rest of this section.

The on-orbit performance of the JFET's is predicted to be limited by proton bombardment of the small-gate JFET. Implantation of the JFET conduction channel has the potential to seriously degrade the noise performance of the JFET and thus degrade the performance of that detector. Traditionally, JFET's are considered relatively radiation hard and these JFET's are no exception. The JFET will continue to operate even after a substantial radiation dose but a degradation in the noise performance could quickly move the XRS detector system from being detector-noise limited to being amplifier-noise limited. For example, figure 45 shows the broadband noise of the detector channels at 1.2 K on-orbit shortly after launch. The broadband noise is between 4 and $6\,\mathrm{nV\,Hz^{-1/2}}$. This is composed of $\sim 2\,\mathrm{nV\,Hz^{-1/2}}$ of detector Johnson noise and 4–5 $\mathrm{nV\,Hz^{-1/2}}$ of noise from the JFET's. For comparison, the in-flight noise at 60 mK is shown in figure 46. Here the detector noise dominates with a white noise level of $\sim 18\,\mathrm{nV\,Hz^{-1/2}}$ at most frequencies and a small bump at frequencies below 100 Hz. The low-frequency bump is due to fluctuations in the detector frame temperature caused by cosmic-ray heating. In figure 46, the phonon and Johnson noise of the detector system contributes $\sim 17\,\mathrm{nV\,Hz^{-1/2}}$ and the JFET amplifier 4–5 $\mathrm{nV\,Hz^{-1/2}}$. In this situation we are detector-noise limited, which is by design. However, if the noise performance of the JFET's were to degrade to an equivalent level as the detector noise, then the spectral resolving power of the associated detector channel would degrade by 40%.

The noise spectra after 11 months on-orbit is shown in figure 47. Here the broadband noise level is higher than in figure 45 due to the loss of helium cryogen and the resulting higher detector temperature and associated Johnson noise. Since 2005 August, the detector system has been in thermal equilibrium with the solid-neon cryogen tank at 15 K. In this case the broadband noise of the detector system is around 8–9 $\mathrm{nV\,Hz^{-1/2}}$ on the majority of channels. The noise is composed of the 4–5 $\mathrm{nV\,Hz^{-1/2}}$ from the JFET's and $7\,\mathrm{nV\,Hz^{-1/2}}$ of Johnson noise from the detectors which are nominally 60 kΩ at 15 K. Thus, on the majority of channels there is no change in the white-noise level or the $1/f$-noise

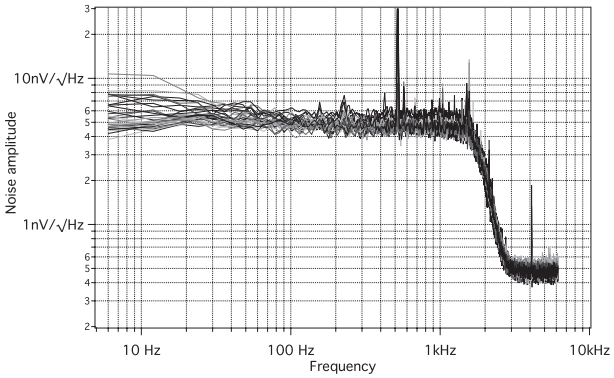

Fig. 45. Noise spectra of the detectors and first stage JFET amplifiers 10 days after launch with the detector system at 1.2 K and the JFET preamplifiers at 130 K. The detectors contribute $2\,\mathrm{nV\,Hz^{-1/2}}$ and the JFET's 4–5 $\mathrm{nV\,Hz^{-1/2}}$ to the white noise level. The signal is rolled off with an 8 pole low pass filter at 2 kHz in the CDP.

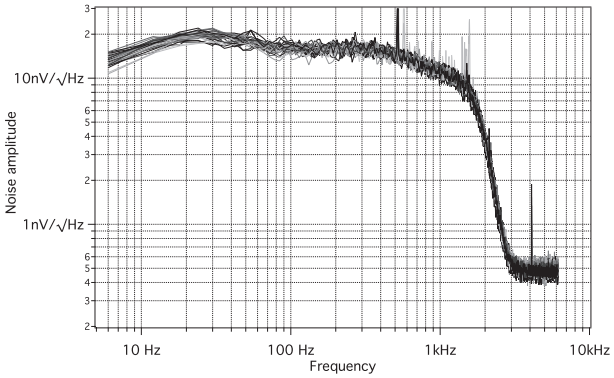

Fig. 46. Noise spectra 12 days after launch with the detector system fully operational at 60 mK and the JFET preamplifiers at 130 K. Here phonon and Johnson noise contribute $\sim 17\,\mathrm{nV\,Hz^{-1/2}}$ and the JFET's 4–5 $\mathrm{nV\,Hz^{-1/2}}$. The "bump" below 100 Hz is due to fluctuations in the detector frame temperature caused by cosmic-ray heating.

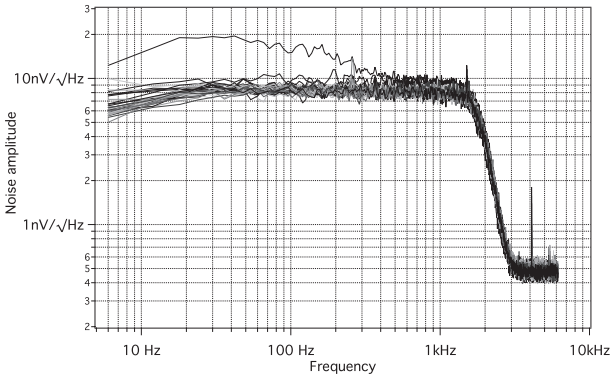

Fig. 47. Noise spectra of the detectors and JFET preamplifiers 11 months after launch. Here the detectors are at 15 K and contribute $7\,\mathrm{nV\,Hz^{-1/2}}$ of Johnson noise and the JFET preamplifiers 4–5 $\mathrm{nV\,Hz^{-1/2}}$. Note that there is clearly one channel that is an outlier that is described in the text.

level of the JFET's in flight. There are three exceptions out of 31 JFET's. One of the exceptions has non-stationary $1/f$ noise. On some measurements there is an enhanced $1/f$ noise at about $15\,\mathrm{nV\,Hz^{-1/2}}$ below 20 Hz and on other measurements it is absent. This is unlikely to be due to a degradation of the JFET and is more probably due to electrical interference with the spacecraft. Two other channels show additional white noise of 9.5 and $11.5\,\mathrm{nV\,Hz^{1/2}}$. These levels are also non-stationary and have actually decreased in the last six months. This is also not likely to be JFET degradation for two reasons. First the fact that the noise level is not monotonically increasing suggests that it is unlikely to be one or more implantation events. Second, the temperature control system on the JFET assembly containing these two JFET's is unable to maintain temperature control with the continued neon gas loading in the cryostat. Thus the temperature of the JFET box is not stable and varies between 126 and 129 K. We know that the noise performance of the JFET's degrades rapidly with temperature below 130 K as the carriers begin to freeze out in the device. The other JFET assembly, which has a slightly lower conductance to the cryostat, has sufficient heater power to maintain temperature control at 130 K. This set of 16 channels shows no increase in the white noise level. Taken at face value, however, the two channels with increased white noise would have degraded the detector resolution by 1 and 9%.

In conclusion, the Front End Assembly performs nominally on orbit with little or no change from its pre-launch performance. Three JFET amplifiers show slight performance degradation after one year on-orbit, but this is unlikely to be due to radiation damage to the amplifiers. Degraded temperature control due to neon loading in the vacuum jacket and minor spacecraft interference are likely causes. In the worst case, where the degradation would be due to radiation damage, this represents a minor degradation of 10% of the channels per year. In addition, since increased noise is likely due to a single implantation event, 90% of the JFET's are demonstrably undamaged. Thus, the XRS has demonstrated the suitability of low-noise, small gate, cryogenic JFET amplifiers in space.

11. Summary

Although the short life span of the XRS is obviously a setback for celestial X-ray spectroscopy, it is hopefully a temporary one, and future implementations of this technology will benefit from the design and on-orbit performance of the Suzaku/XRS. The solid Ne is expected to last through 2007 and during this time the mechanical cooler and instrument electronics will continue to be operated. This will extend the baseline for valuable engineering data that should benefit future low-temperature missions.

The authors wish to thank the referee for carefully reading the lengthy manuscript and offering many ways to significantly improve it, and for catching several errors. The authors are extremely grateful to hundreds of technicians, engineers, scientists, managers, and students who made the XRS possible. These include team members that contributed to the original design of the XRS and all of the efforts to successfully propose for and develop the XRS on Suzaku. In particular,

we are extremely grateful for the significant contributions of the following team members:

NASA/Goddard Space Flight Center: Gustave Comeyne, Bernie Klein, John Leon, Dino Machi, Don Margolies, and James Murphy for their management of the XRS instrument.

Charlie Adams, Lorella Angelini, Dale Arbogast, Keith Arnaud, Shanta Arur, Bob Baker, Chris Baluta, Willie Barber, Christine Baxley, Jason Behr, John Bichell, Dave Bloom, Garcia Blount, Regis Brekosky, Stephen Buchner, Ed Canavan, Phil Chen, Chuck Chidekel, Ron Colvin, Tony Comberiate, Jeff Condron, Tom Corris, Allen Crane, John Crow, Steve Derdeyn, Norm Dobson, Jeff Dumonthier, Mitra Dutta, Ken Ebisawa, Robert Edmonds, Rick Eichen, Dino Fasce, Enectali Figueroa-Feliciano, Charlie Fleetwood, Mike Flick, John Francis, Massimiliano Galeazzi, Joe Generie, Chris Gonzalez, Walt Goodale, Phil Goodwin, Marsha Gosselin, Steve Graham, Darrell Gretz, Fred Gross, John Gygax, Tom Hait, Christina Hammock, Chuck Hanchak, Holly Hancock, Tom Hanyok, Steven Harper, Ilana Harrus, John Harvey, Dave Huff, Nino Ingegneri, Sandra Irish, Harold Isenberg, Cliff Jackson, Mindy Jacobson, John Kearney, Linda Kearney, Jonathan King, Ron Kolecki, Evan Kunes, Michelle Lacombe, Juli Lander, Mike Lenz, Dahai Liu, Jim Lochner, James Loughlin, Ron Martin, Richard McClanahan, Leo McConville, Mickey McDonald, Chris Miller, Christine Miranda, Herb Mittlemman, Anna Montoro, Carol Mosier, Theo Muench, Koji Mukai, Scott Murphy, Richard Mushotzky, Philip Myers, Son Ngo, Curtis Odell, Jeanne Palmer, Bill Pence, Frank Peters, Rob Petre, Ed Pier, Veronica Ponce, Ed Quinn, Joe Radich, John Rauscher, Marco Rosales, Brian Ross, Mike Ryschkewitsch, Tarek Saab, Marc SanSebastian, Carol Sappington, Sandy Schumann, Sharon Seiple, Noman Siddiqi, Ken Simms, Randall Smith, Carl Stahle, Darrell Story, John Sutton, Louis Thomas, David Turnbo, Jim Tuttle, Brent Warner, Nicholas White, Crystal White, Maxine Windhausen, George Winkert, George Wofford, Steve Wood, Gerry Wright, Debbie Yodder and John Zahniser for designing, building, and providing guidance to the XRS hardware and science program.

Department of Physics, University of Wisconsin: Nick Bilgri, Ethan Feldman, Lindsay Rocks, Wilt Sanders, John Vaillancourt, and Gaudenis Vidugiris for the development of the flight internal calibration source and contributions to the microcalorimeter design.

Space Science Engineering Center, University of Wisconsin: Bob Paulos for overseeing and providing rapid delivery of the ADR saltpill.

Luxel Corporation: Forbes Powell for working closely with Goddard to develop the X-ray blocking filters.

NASA Headquarters: Alan Bunner, Paul Hertz, and Louis Kaluzienski for their efforts to make the XRS and the Suzaku program a reality, and their continuous support of the Suzaku US Guest Investigator Program. Also Steve Horowitz, Adriana Ocampo, and Alan Smale for program and international support.

ISAS/JAXA: Prof. Kenji Minesugi for mechanical design of the neon dewar.

Sumitomo Heavy Industries, Ltd.: Makoto Kyoya, Seiji Yoshida, Keisuke Tsurumi, Yoshiyuki Kimura, Takeshi Hiroishi, Isao Gonda, Yoshinobu Ochi, Yumiki Ochi, Yuji Tarumi, Junji Seno, Kenji Okamoto, Shoji Tsunematsu, Shunji Hoshika, Kiyomi Otsuka, Yoji Fujioka, Jun'ichi Inoue, Shizuo Miyawaki, Norihisa Itoh, Sanae Takahashi for fabrication and testing of the dewar.

NEC TOSHIBA Space Systems, Ltd.: Kenji Kitade, Takayuki Tohma, Kazuyo Mizushima for the spacecraft interface and overall testing on spacecraft, Teiji Yoshida, Toshimitsu Nakayama, Hisashi Harada for fabrication of the power supply unit, and Akira Fukatsu, Takuji Nakano, Taku Saito, Hiroaki Nishio, Hideki Takei for fabrication of the filter wheel.

Fujitsu, Inc.: Keiji Satoh, Kohji Hayashi, Keitaro Ohno for fabrication of the Astro-E XRS-DE.

Mitsubishi Heavy Industries, Ltd.: Naoki Shibayama, Yoshikatsu Kuroda, Makio Yamaguchi, Atsushi Nakajima, Kazunori Masukawa, Keigo Saso, Shigeo Kasai for fabrication of the Astro-E2 XRS-DE.

SHI Examination & Inspection, Ltd.: Akira Nagano for fabrication of ^{41}Ca sources.

Takeshi Toramatsu, Akira Hayakawa, Chiaki Inoue at Tokyo Metropolitan University for calibration of the filter wheel, and Toshiyuki Miyazaki, Tai Oshima, Masahiro Yamazaki, Akihiro Kushino, Teru Ishikawa, Yuichiro Ezoe, Kiyonori Yoshida, Akihiro Tsuchiya, Kensuke Masui, Tomotaka Yoshino, Toshishige Hagihara, Kosuke Sato, Tamayuki Fujimori, Akio Hoshino, Yoshiyuki Yamakawa, and post-docs/graduate students at ISAS/JAXA and Tokyo Metropolitan University who supported testing and monitoring of the dewar for a long time until launch.

Work by the U.C. LLNL was performed under the auspices of the D.o.E. under contract No. W-7405-Eng-48. Work by Tokyo Metropolitan University and ISAS/JAXA was partially supported by the Ministry of Education, Culture, Sports, Science, and Technology of Japan, Grant-in-Aid for Scientific Research No. 14079103 and 15001002. N.O. was supported in part by RIKEN President's Discretionary Fund No. 88120.

References

Aschenbach, B. 1988, Appl. Opt., 27, 1404
Audley, M. D., et al. 1999, Proc. SPIE, 3765, 751
Bavdaz, M., Lumb, D., Gerlach, L., Parmar, A., & Peacock, A. 2005, Proc. SPIE, 5898, 58980A
Beiersdorfer, P. 2003, ARA&A, 41, 343
Beiersdorfer, P., et al. 2003, Science, 300, 1558
Boyce, K. R., et al. 1999, Proc. SPIE, 3765, 741
Brekosky, R. P., et al. 2004, Nucl. Instrum. Methods Phys. Res. A, 520, 439

Breon, S., DiPirro, M. J., Tuttle, J. G., Shirron, P. J., Warner, B. A., Boyle, R. F., & Canavan, E. R. 2000, Adv. Cryo. Eng., 45, 507
Brinkman, A. C., et al. 2000, ApJ, 530, L111
Brown, G. V., et al. 2006a, Phys. Rev. Lett., 96, 253201
Brown, G. V., et al. 2006b, Nucl. Instrum. Methods Phys. Res. A, 559, 623
Canavan, E. R., Tuttle, J. G., Shirron, P. J., & DiPirro, M. J. 2000, Adv. Cryo. Eng., 45, 545
Canizares, C. R., et al. 2000, ApJ, 539, L41
Chen, H., et al. 2005, ApJ, 618, 1086
Cottam, J., et al. 2004, Nucl. Instrum. Methods Phys. Res. A, 520, 368
Cottam, J., et al. 2006, Nucl. Instrum. Methods Phys. Res. A, 559, 617
den Herder, J. W., et al. 2001, A&A, 365, L7
DiPirro, M. J., Shirron, P. J., & Tuttle, J. G. 1994, Adv. Cryo. Eng., 39, 129
Fujimoto, R., Mitsuda, K., Hirabayashi, M., Narasaki, K., Breon, S., Boyle, R., DiPirro, M., Volz, S. M., & Kelley, R. L. 2006, Nucl. Instrum. Methods Phys. Res. A, 559, 648
Furusho, T., et al. 1999, Proc. SPIE, 3765, 664
Garmire, G. P. 1999, BAAS, 31, 1515
Gendreau, K. C. 1995, PhD Thesis, Massachusetts Institute of Technology
Gendreau, K. C., et al. 1999, Proc. SPIE, 3765, 137
Han, S.-I., et al. 1998, Proc. SPIE, 3445, 640
Henke, B. L., Gullikson, E. M., & Davis, J. C. 1993, Atomic Data and Nuclear Data Tables, 54, 181
Irwin, K. D. 2002, Physica C, 368, 203
Jansen, F., et al. 2001, A&A, 365, L1
Kelley, R. L., et al. 1999, Proc. SPIE, 3765, 114
Kelley, R. L., Moseley, S. H., Stahle, C. K., Szymkowiak, A. E., Juda, M., McCammon, D., & Zhang, J. 1993, J. Low Temper. Phys., 93, 225
Kilbourne, C. A. 2004, Nucl. Instrum. Methods Phys. Res. A, 520, 402
Kilbourne, C. A., et al. 2006, Nucl. Instrum. Methods Phys. Res. A, 559, 620
Koyama, K., et al. 2007, 59, S23
McCammon, D., et al. 2002, ApJ, 576, 188
McCammon, D. 2005, in Topics in Applied Physics 99, ed. C. Enss (Heidelberg: Springer), 1
Mitsuda, K., et al. 2007, PASJ, 59, S1
Mitsuda, K., & Kelley, R. 1999, Nucl. Instrum. Methods Phys. Res. A, 436, 212
Moseley, S. H., Mather, J. C., & McCammon, D. 1984, J. Ap. Phys., 56, 1257
Nagamatsu, J., Nakagawa, N., Muranaka, T., Zenitani, Y., & Akimitsu, J. 2001, Nature, 410, 63
Narasaki, K., Tsunematsu, S., Kanao, K., Otsuka, K., Hoshika, S., Fujioka, K., Tsurumi, K., & Hirabayashi, M. 2006, Adv. Cryo. Eng., 51, 1505
Neugebauer, G., et al. 1984, ApJ, 278, L1
Ota, N., et al. 2006, Nucl. Instrum. Methods Phys. Res. A, 559, 614
Panek, J. S., Tuttle, J. G., Marrero, V., Mustafi, S., Edmonds, R., Gray, A., & Riall, S. 2004, Adv. Cryo. Eng., 49, 952
Porter, F. S., et al. 1999, Proc. SPIE, 3765, 729
Porter, F. S., et al. 2000, Proc. SPIE, 4140, 407
Porter, F. S., et al. 2004, Rev. Sci. Instrum., 75, 3772
Porter, F. S., Brown, G. V., & Cottam, J. 2005, in Cryogenic Particle Detection, ed. C. Enss (Heidelberg: Springer), 359
Saab, T., et al. 2004, Proc. SPIE, 5505, 320
Schlachter, S. I., Goldacker, W., Frank, A., Ringsdorf, B., & Orschulkom, H. 2006, Cryogenics, 46, 201
Serlemitsos, P. J., et al. 1995, PASJ, 47, 105
Serlemitsos, P. J., et al. 2007, PASJ, 59, S9
Serlemitsos, A. T., Warner, B. A., SanSebastian, M., & Kunes, E. 1990, Proc. SPIE, 1340, 303
Shirron, P. J., & DiPirro, M. J. 1998, Adv. Cryo. Eng., 43, 949
Shirron, P. J., DiPirro, M. J., Panek, J., Kelley, R., Mitsuda, K, Fujimoto, R., Hirabayashi, M., & McCammon, D. 2006, Nucl. Instrum. Methods Phys. Res. A, 559, 666
Silver, E., et al. 2002, AIP Conf. Proc., 605, 555
Stahle, C. K., et al. 1999, Proc. SPIE, 3765, 128
Stahle, C. K., et al. 2003, Proc. SPIE, 4851, 1394
Stahle, C. K., McCammon, D., & Irwin, K. D. 1999, Physics Today, 32
Strüder, L., et al. 2001, A&A, 365, L18
Szymkowiak, A. E., Kelley, R. L., Moseley, S. H., & Stahle, C. K. 1993, J. Low Temper. Phys., 93, 281
Takahashi, T., et al. 2007, PASJ, 59, S35
Takahashi, T., Mitsuda, K., & Kunieda, H. 2006, Proc. SPIE, 6266, 62660D
Turner, M. J. L., et al. 2001, A&A, 365, L27
Tuttle, J. G., Hait, T. P., Boyle, R. F., Muller, H. J., Hodge, J. D., & Breon, S. R. 1998, Adv. Cryo. Eng., 43, 965
Volz, S. M., Mitsuda, K., Inoue, H., Ogawara, Y., Hirabayashi, M., & Kyoya, M. 1996, Cryogenics, 36, 763
Weisskopf, M. C., Brinkman, B., Canizares, C., Garmire, G., Murray, S., & van Speybroeck, L. P. 2002, PASP, 114, 1
White, N. E., Tananbaum, H., Weaver, K., Petre, R., & Bookbinder, J. A. 2004, Proc. SPIE, 5488, 382